Article:
Arribas Perez, M orcid.org/0000-0002-6489-5857 and Beales, PA orcid.org/0000-0001-9076-9793 (2021) Biomimetic Curvature and Tension-Driven Membrane Fusion Induced by Silica Nanoparticles. Langmuir, 37 (47). pp. 13917-13931. ISSN 0743-7463

https://doi.org/10.1021/acs.langmuir.1c02492

Biomimetic curvature and tension-driven membrane fusion induced by silica nanoparticles

Marcos Arribas Perez[1] *and Paul A. Beales*[1,2,*]

[1] Astbury Centre for Structural Molecular Biology and School of Chemistry, University of Leeds, Leeds, LS2 9JT, UK.

[2] Bragg Centre for Materials Research, University of Leeds, Leeds, LS2 9JT, UK.

* Correspondence: p.a.beales@leeds.ac.uk

Abstract

Fusion events in living cells are intricate phenomena that require the coordinate action of multicomponent protein complexes. However, simpler synthetic tools to control membrane fusion in artificial cells are highly desirable. Native membrane fusion machinery mediates fusion driving a delicate balance of membrane curvature and tension between two closely apposed membranes. Here we show that silica nanoparticles (SiO_2 NPs) at a size close to the cross-over between tension-driven and curvature-driven interaction regimes initiate efficient fusion of biomimetic model membranes. Fusion efficiency and mechanisms are studied by Förster Resonance Energy Transfer (FRET) and confocal fluorescence microscopy. SiO_2 NPs induce a slight increase in lipid packing likely to increase the lateral tension of the membrane. We observe a connection between membrane tension and fusion efficiency. Finally, real-time confocal fluorescence microscopy reveals three distinct mechanistic pathways for membrane fusion. SiO_2 NPs show significant potential for inclusion in the synthetic biology toolkit for membrane remodelling and fusion in artificial cells.

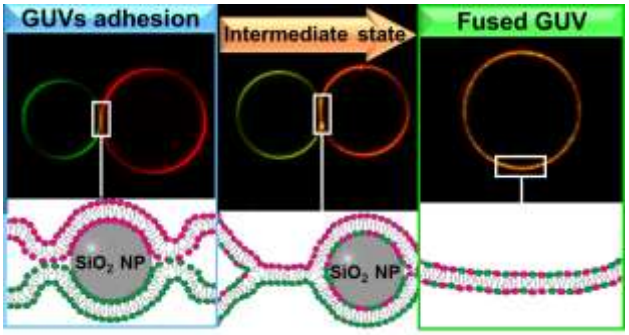

Keywords: artificial cells, membrane remodelling, bionanotechnology, lipid bilayers, lipid mixing, membrane biophysics.

INTRODUCTION

Membrane fusion is a key communication and transport process in living cells that is highly desirable to replicate in artificial cell systems to control chemical compartmentalisation and trigger targeted chemical processes. The life of cells is largely dependent on membrane fusion processes. Eukaryotic cells require sequential fusion events to transport substances between membrane-bound organelles, to release molecules to the extracellular environment or to incorporate nutrients *via* endocytosis. [1-2]

Cell-sized giant unilamellar vesicles (GUVs) are common model architectures used in synthetic biology as plasma membrane mimics. [3-4] Due to their ability to reproduce biological processes, these minimal protocells are excellent platforms for the study of complex biological processes (*e.g.* membrane fusion) in a simpler context. [5-6] Furthermore, these artificial systems can encapsulate chemical reactions with potential biotechnological applications. [7-10] Therefore, membrane fusion can be exploited to modify the composition of the membrane, the volume, surface area and shape of the vesicle as well as to trigger chemical reactions and complex metabolic cascades by delivering energy sources, enzymes, protein complexes or chemical substrates into the lumen of the artificial cell. [11-13]

Mechanistic models for membrane fusion involve a series of sequential intermediate steps. The process begins with the docking of two membranes. This is followed by the destabilisation of the lipids by inducing these membranes to curve towards each other and increasing their local lateral tension. This leads to the hemifusion of the contacting outer leaflets followed by the final formation and expansion of a full fusion pore, which completes the process. [14-15] In living cells, membrane fusion is regulated and catalysed by the coordinated action of protein complexes, among which the SNARE proteins are possibly the best known. [2] However, proteins are not essential to trigger membrane fusion of lipid vesicles *in vitro*. Protein-free membrane fusion can be achieved using other chemical stimuli, including particular membrane compositions, [16-17]

membrane-anchored DNA, [18] peptides [19-20] and multivalent ions [21] or by physical stimuli such as optically heated gold nanoparticles, [22-24] or electric pulses. [25] All these fusion strategies (including proteins) share the ability to induce one or more changes in membrane tension, curvature, fluidity, or other biophysical properties of the membrane which can lower the energy barrier to membrane fusion with varying degrees of efficiency. The ability of engineered nanoparticles (NPs) to deform membranes and facilitate remodelling processes can also be exploited in synthetic biology to efficiently trigger and control membrane fusion. An example of a NP-based fusion system has been recently presented by Tahir *et al*. who designed amphiphilic nanoparticles composed of a gold core functionalized with a mixed monolayer of alkanethiol ligands able to perform calcium-triggered membrane fusion [26].

The mechanism of interaction between NPs and lipid membranes is determined by a balance between the adhesion energy (*w)*, which attracts the NPs into the membrane, and the membrane's resistance to deformation, which opposes the membrane wrapping around the spherical NPs, defined by the elastic properties of the membrane. Assuming a tensionless membrane, the ratio between the bending rigidity (κ) of the membrane and the adhesion energy defines a critical diameter (d_c) above which the NP is spontaneously wrapped by the membrane: [27]

$$d_c = 2\sqrt{\left(\frac{2\kappa}{w}\right)} \qquad (1)$$

According to this simple model, a nanoparticle of a given size will be completely wrapped by the membrane only if the adhesion energy is high enough to overcome the energy cost needed to bend the membrane. However, there are intermediate states where NPs only get partially wrapped by the membrane. The degree of wrapping is thought to be limited by the membrane tension, which represent an additional energy cost that has to be overcome by the adhesion energy to achieve full wrapping [28-30]. The adhesion energy is often difficult to evaluate as it is the

results of a combination of several forces acting together at the nanoparticle-membrane interface, including hydration forces, van der Waals, electrostatic, and steric interactions. [31] These forces can also be influenced by the properties of the medium where the interaction occurs [32] and can lead to a cooperative behaviour of the NPs. For instance, Contini *et al.* have reported that gold nanoparticles (AuNPs) with a diameter equal to or below 10 nm undergo cooperative absorption and can form tubular deformations in the membrane, while the adsorption and ability to bend membranes of larger AuNPs is significantly reduced. [29]

The interaction SiO_2 NPs and lipid membranes has been reported to be dependent on the NP size. Cryo-electron microscopy and tomography images have shown that SiO_2 NPs with diameter larger than 30 nm are totally wrapped by DOPC membranes and internalised into large unilamellar vesicles LUVs, while SiO_2 NPs of 15 nm remain attached to the LUV surface but are not engulfed by the membrane [33]. In a different study, Zhang *et al* showed that SiO_2 NPs of 18 nm diameter interact with DOPC giant unilamellar vesicles (GUVs) inducing high tension, solidification and rupture of lipid membranes, whereas larger SiO_2 NPs of 78 nm and 182 nm are wrapped by the membrane [34]. In that study they propose that a cross-over between both effects will be observed when the membrane adhesion and curvature elastic energies become equal, that is when the size of the SiO_2 NPs equals the critical diameter. Introducing typical values of bending rigidity of DOPC membranes (19-24 $\kappa_B T$)[35-36] and the adhesion energy between SiO_2 and phosphocholine (PC) membranes (0.5 and 1 mJ/m^2) [37] in equation 1 renders a critical diameter in the range of 25-40 nm.

In this work, we introduce silica nanoparticles (SiO_2 NPs) as a potential tool to induce fusion of biomimetic lipid membranes. We hypothesise that SiO_2 NPs within the critical size range will provide a balance between membrane curvature and membrane tension analogous to the physical membrane perturbations induced by natural membrane fusion complexes. Hence, we investigate the potential for 30 nm diameter SiO_2 NPs as artificial membrane fusion machinery.

The efficiency of these SiO_2 NPs in promoting lipid mixing, considered an essential consequence of membrane fusion events, in populations of LUVs is studied using a Förster Resonance Energy Transfer (FRET) assay. However, this method is insufficient to investigate the mechanisms involved in fusion events. For this reason, we perform further confocal microscopy studies GUVs, which allow time-resolved investigation of the trajectories of fusion events between individual pairs of GUVs. Direct imaging of kinetic pathways of membrane fusion permits identification of intermediate fusion states and quantification of the rate of lipid mixing between fusing GUVs in order to propose a mechanistic interpretation of the process.

RESULTS AND DISCUSSION

SiO_2 NPs characterisation

The SiO_2 NPs employed in this investigation are nanospheres of 30.8 ± 3.9 nm diameter as characterised by Transmission Electron Microscopy (Figure S1). A similar size distribution is observed using Dynamic Light Scattering (DLS) (Table S1). DLS measurements also show that the SiO_2 NPs are colloidally stable in the experimental buffer (20 mM HEPES, 150 mM NaCl, at pH 7.4) for at least 48 h (Figure S2), a time much longer than any of the experiments presented below. Thus, these SiO_2 NPs have appropriate colloidal stability to investigate their application as a trigger for membrane fusion. These SiO_2 NPs are negatively charged as indicated by their zeta (ζ) potential (-18.2 ± 1.8 mV) determined using Dynamic Electrophoretic Light Scattering Analysis (DELSA).

SiO_2 NPs induce intervesicular lipid mixing

The fusogenic activity of SiO_2 NPs is initially evaluated by a lipid mixing assay based on FRET. [38] DOPC LUVs labelled with both NBD-DOPE and Rh-DOPE are mixed with probe-free DOPC LUVs at a 1:5 ratio and exposed to different concentrations of SiO_2 NPs for 30 min. The

values for full lipid mixing are obtained from samples containing only LUVs labelled with 0.05 mol% NBD-DOPE and Rh-DOPE, which represent the maximum dilution of the probes in the membrane that can be reached in our experiments.

The samples not treated with SiO_2 NPs show a maximum FRET ratio because both fluorophores are closely colocalised in the labelled LUVs. However, the exposure to SiO_2 NPs induce a decrease in FRET ratio, which is indicative of dose-dependent lipid mixing between vesicles (Figure S3). Our results show that nearly 50% lipid mixing is reached when the LUVs are incubated with 30 µg/ml SiO_2 NPs and around 80% lipid mixing happens when LUVs are exposed to 100 µg/ml SiO_2 NPs (Figure 1a). The presence of SiO_2 NPs in solution promotes the exchange of lipids between labelled and unlabelled LUVs, hence the distance between the donor and acceptor fluorophores increases as they get diluted into the unlabelled membranes and the FRET signal drops. However, these results must be interpreted carefully since the changes in FRET signal are not exclusively produced by fusion but can result from other processes such as hemifusion [39] and rupture of the vesicles. [40]

The complete fusion of liposomes upon interaction with SiO_2 NPs would lead to a larger population of vesicles. Hence, we used DLS to measure changes in the hydrodynamic size of LUVs after exposure to SiO_2 NPs with the aim to assess whether SiO_2 NPs induce complete fusion of LUVs. We observe that the size distribution of LUVs increases after incubation with 30 µg/ml and 100 µg/ml SiO_2 NPs for 30 min from 347.40 ± 14.05 nm to 482.90 ± 52.02 nm and 564.10 ± 23.23 nm, respectively, thus a large proportion of the LUVs in the sample has fused into larger vesicles (Figure 1b, Table S1). Assuming that vesicle volumes are conserved during fusion events, these increases in vesicle size distributions are equivalent to, on average, 2.7 vesicles (30 µg/ml) and 4.3 vesicles (100 µg/ml) fusing with one another to form the larger vesicle population. These estimates are consistent with the 50% and 80% lipid mixing values reported by

FRET at these NP concentrations when starting from an initial 1:4 mixture of labelled to unlabelled vesicles.

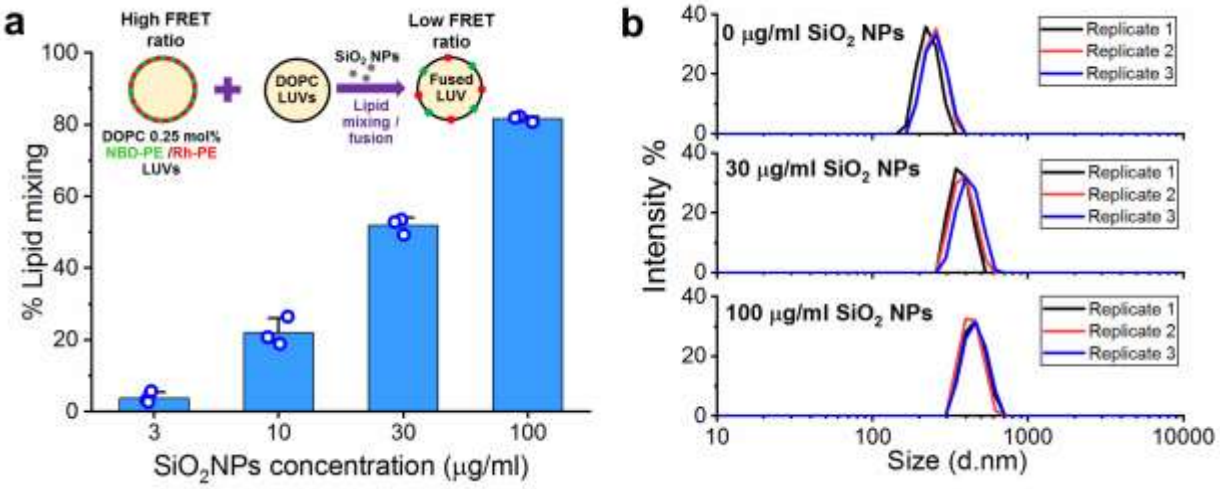

Figure 1. a) Percentage of lipid mixing induced by SiO_2 NPs obtained by FRET. Lipid mixing is detected as a decrease of FRET ratio in samples containing unlabelled DOPC LUVs and DOPC LUVs labelled with NBD-DOPE and rhodamine-DOPE (inset). The lipid mixing rises as the LUVs population is exposed to increased concentrations of SiO_2 NPs. b) Hydrodynamic size distribution of DOPC LUVs before (0 μg/ml SiO_2 NPs) and after exposure to 30 μg/ml and 100 μg/ml SiO_2 NPs for 30 minutes measured by DLS. After incubation with SiO_2 NPs the size of the LUVs increases.

SiO_2 NPs induce fusion of GUVs

Next, we used confocal microscopy to directly observe the ability of SiO_2 NPs to promote fusion of DOPC GUVs. Initially, we recorded the fate of GUVs labelled with 0.5 mol% Rh-DOPE (Rh-GUVs) after exposure to 25 μg/ml SiO_2 NPs. Importantly, our observations clearly confirm the ability of SiO_2 NPs to trigger fusion of apposing GUVs, but not all the fusion events occur in the same manner. We observe that various processes, involving distinct morphological changes of GUVs, can lead to membrane fusion (Figure 2a and 2b, Supplementary movies 1 and 2).

Figure 2a shows a sequence of two fusion processes occurring between two apposed GUVs, one of them with a third GUV inside. Initially, one of the GUVs begins to shrink and its membrane is apparently transferred to the neighbour GUV which progressively gets bigger. At

the same time, the third GUV, which was inside the growing one, is expelled from the lumen. These two GUVs remain attached to each other and slowly get smaller until eventually their membranes fuse resulting in a single final GUV (Supplementary Movie 1). During the process, we observe spots in the GUV surface with a fluorescence signal considerably brighter than the rest of the membrane. This enhanced localised fluorescence intensity is attributed to highly curved regions of the membrane induced by the NPs adhering to the GUV surface and being wrapped by the membrane. [34, 41] The nanoscale membrane curvature induces an increased membrane area, and therefore number of fluorophores, per pixel in the x-y plane of the image, which translates into brighter fluorescent signal. If NPs get fully wrapped by the membrane, they can lead to fission processes through which they pull the membrane which engulfs them out from the GUV membrane. [41-42] These fission processes explain the fluorescence signal observed in the lumen of the GUVs in Figure 2a. A different mechanism is observed in Figure 2b, where the fusion occurs after the sudden breakage of the membrane at one end of the GUV contact region. The part of the membrane where the GUVs were in contact gets trapped in the lumen of the new fused GUV and quickly rearranges to form an intraluminal vesicle (Supplementary Movie 2).

In Figures 2a and 2b, we observe an increase of the fluorescence intensity at the vertices of the membrane interface which separates the GUVs. This local rise in fluorescence intensity likely denotes that three bilayers are contacting at these points (Y-like junction), one bilayer from each GUV and a mixed bilayer formed at the interface, commonly named as hemifusion diaphragm. In these junctions, the membranes are under a high curvature stress and the lipids are condensed and tightly packed showing enhanced fluorescence. The formation of intermediate fusion states and other mechanistic aspects of the fusion process will be discussed in more detail later.

In order to observe whether the contents of the DOPC GUVs mix upon vesicle fusion, we carried out additional experiments mixing a population of GUVs encapsulating a sucrose solution

with a second GUV population containing a mixture of sucrose and fluorescent 70 kDa TRITC-dextran (TRITC-filled GUV). By analysing the fluorescence intensity of the GUV cargo during the fusion process we observed that the fusion triggered by SiO_2 lead to a complete mix of the lumens of the GUVs (Figure 2c, Supplementary movie 3). Before the GUVs fully fuse, there is a lipid transfer between the GUVs which results in the simultaneous swelling of the fluorescently loaded vesicle and shrinking of the contiguous GUV. This swelling requires the entry of non-fluorescent content into the TRITC-filled GUV which causes a gradual dilution of the TRITC in the lumen and explains the gradual drop of its fluorescent observed before the GUVs fully fuse. By comparing the fluorescence intensity in the lumen of the TRITC-filled GUV with its volume at the different time points, we clearly observe that the increase of the TRITC-filled GUV volume is proportional to the drop of the fluorescence intensity in its lumen (Figure 2c). However, it is unclear whether the swelling is driven by the net influx of contents into the TRITC-filled GUV from the shrinking GUV, from the outer medium or both, through transient nanopores opened in the membrane. During the swelling process we do not observe transfer of TRITC-dextran from the growing GUV to the shrinking GUV until the fusion pore opens. Once the GUVs fuse, the lumens of the two GUVs mix completely, consequently the fluorescent dextran molecules get diluted in the final lumen and the fluorescent intensity of the GUV cargo decreases steeply. (Figure 2c).

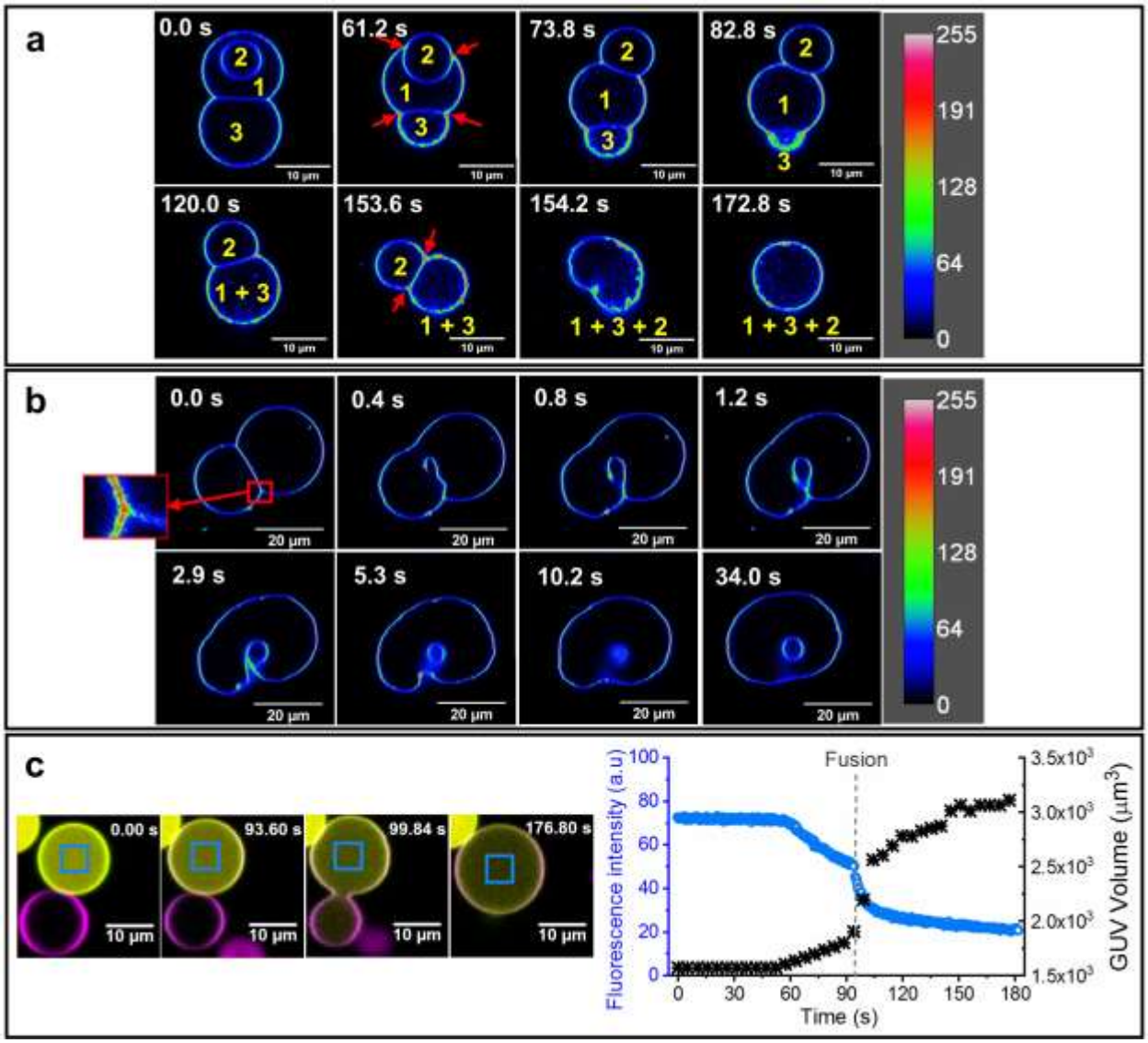

Figure 2. Confocal microscopy images of fusion processes of GUVs triggered upon exposure to 25 µg/ml SiO_2 NPs. In panels a and b, GUVs are labelled with of Rh-DOPE and its fluorescence is presented as a pseudocolor associated to the intensity as indicated in the colour code scale. a) Initially two GUVs are docked (1 and 3) and the first one has a third vesicle inside (2). As time progresses, the GUV 3 gradually merges into the GUV 1 and at the same time GUV 2 is ejected. The resulting 1+3 GUV and GUV 2 remain attached and the former start shrinking. Eventually the GUVs fuse originating a single final GUV 1+3+2. b) The boundary membrane which separate the two GUVs suddenly breaks at one end and the GUVs fuse. A membrane fragment gets trapped in the lumen of the new GUV and spontaneously adopt a spherical configuration forming an intralumenal vesicle. Red arrows indicate regions of increased fluorescence intensity observed at the edges of the docking regions. c) Micrographs showing the lumen mixing process during fusion. One of the GUVs, labelled with 1 mol% DiO (green) is loaded with a mixture of sucrose and TRITC-dextran 70 kDa (yellow) and the other is labelled with 1 mol% DiD (magenta) and its lumen contains only sucrose (non-fluorescent). The plot shows the fluorescence intensity of TRITC-dextran (blue circles, blue y-axis) in the region of the GUV lumen indicated by the blue box in the micrographs as well as the volume of the GUV loaded with TRITC-dextran (black crosses, black y-axis) against time. The drop in fluorescence intensity before fusion corresponds with the swelling of the GUV. After fusion, the lumens of the two GUVs mix inducing a sharp drop of fluorescent intensity in the lumen of the resultant GUV.

Influence of lipid packing and membrane tension on fusion processes

In membrane fusion events, lipid packing defects are considered as an initial step required for two adjacent membranes to fuse. [26, 43-44] Since previous studies on NP-membrane interactions have shown that SiO_2 NPs produce perturbations in lipid packing and membrane fluidity, [34, 45-46] we used Laurdan spectral imaging to quantify changes in lipid packing and membrane hydration of DOPC GUVs labelled with 0.5 mol% Laurdan after incubation with 25 µg/ml SiO_2 NPs.

Our results show that SiO_2 NPs induce a mild but statistically significant increase in the average generalised polarisation (GP) of the Laurdan molecules embedded in the membrane (Figure 3a). The increase in GP correspond to a less hydrated membrane with the lipids more tightly packed. The adsorption of the SiO_2 NPs onto the GUVs is likely to create local highly curved deformations in the membrane. These nanoscale deformations are however smaller than the microscope resolution and are not detected in the GP maps, which show homogeneous GP values across the whole GUV membrane (Figure S4). The differences between the GP values at the poles of the GUVs is due to an artifact resulting from the polarisation of the light which produce different fluorescence intensities in the equator and the poles of the GUVs. In addition, the negative surface charge of SiO_2 NPs is likely to alter the tilt angle of the DOPC headgroup dipole leading to a condensation of the lipids and a reduction of the polarity of the membrane which increase the tension of the membrane and facilitate the contact between closely localised membranes. [16, 34, 47-49] The high local membrane curvature along with the increased membrane tension can lead to lipid packing defects and unfavourable exposure of hydrophobic lipid tails to the aqueous environment. These packing defects can be compensated in the contact zone between two membranes as the exposed lipid tails of the inner monolayer of one membrane can match the exposed hydrophobic region of the adjacent membrane.

Membrane tension is known to be a crucial biophysical parameter for the progress of membrane fusion events. [48, 50-53] Hence, we investigated the effect of the membrane tension in

the fusion process triggered by SiO_2 NPs. The first step to assess the influence of membrane tension in the fusion process was to modify the tension of the GUVs after electroformation by incubating them in hypertonic, isotonic or hypotonic buffer overnight to obtain “relaxed”, “neutral”, or “tense” GUVs, respectively. Then, to quantify the proportion of GUVs undergoing fusion in the sample we mixed equally tense Rh-GUVs and DiO-GUVs (DOPC labelled with 1 mol% DiO) in a 1:1 volume ratio before adding the SiO_2 NPs (25 µg/ml). Finally, after incubating the GUVs with the NPs for 30 min we took tile scans and counted the proportion of GUVs with both dyes colocalised in the membrane (lipid mixed GUVs).

The images of vesicles incubated in isotonic buffer show an average proportion of lipid mixed and fused GUVs of 12.25 % from the total number of GUVs. The osmotic relaxation of the GUVs reduces the mean proportion of lipid mixed GUVs in the samples to 7.90 %, while in the samples of osmotically tensed GUVs the average percentage of vesicles fusing rises to 15.96 % (Figure 3b). The tile scans were taken from 5 independent samples for each condition. These data denote a clear impact of the membrane tension on the fusion process induced by the SiO_2 NPs. Similar results were obtained for LUVs measured by FRET spectroscopy (Figure S5). In addition to promoting the fusion process itself, membrane tension can facilitate the close apposition of two GUVs by favouring partial NP wrapping over complete engulfment. [29] At the interface between two GUVs, SiO_2 NPs might get partially wrapped by both membranes and promote their adhesion. This idea is supported by a recent study which has shown that gold nanoparticles and silica nanoparticles partially wrapped by the membrane can promote the adhesion of GUVs, while complete wrapping induces vesicle tubulation and collapse. [54]

Note that from the confocal microscopy images we are only counting the fusion events occurring between oppositely labelled GUVs, but fusions between GUVs labelled with the same dye are also taking place. In our samples, a Rh-GUV has the same probability to fuse with a DiO-GUV than with another Rh-GUV, and the same applies for a DiO-GUV. Therefore, the proportion

of GUVs undergoing fusion in our samples is, in theory, double than that quantified in the images. Also note that the proportion of fused GUVs is likely lower than that observed in LUV experiments due to the much larger GUVs exhibiting limited diffusion compared to LUVs, significantly reducing the number of collision events between these vesicles, which are required to facilitate membrane adhesion and fusion.

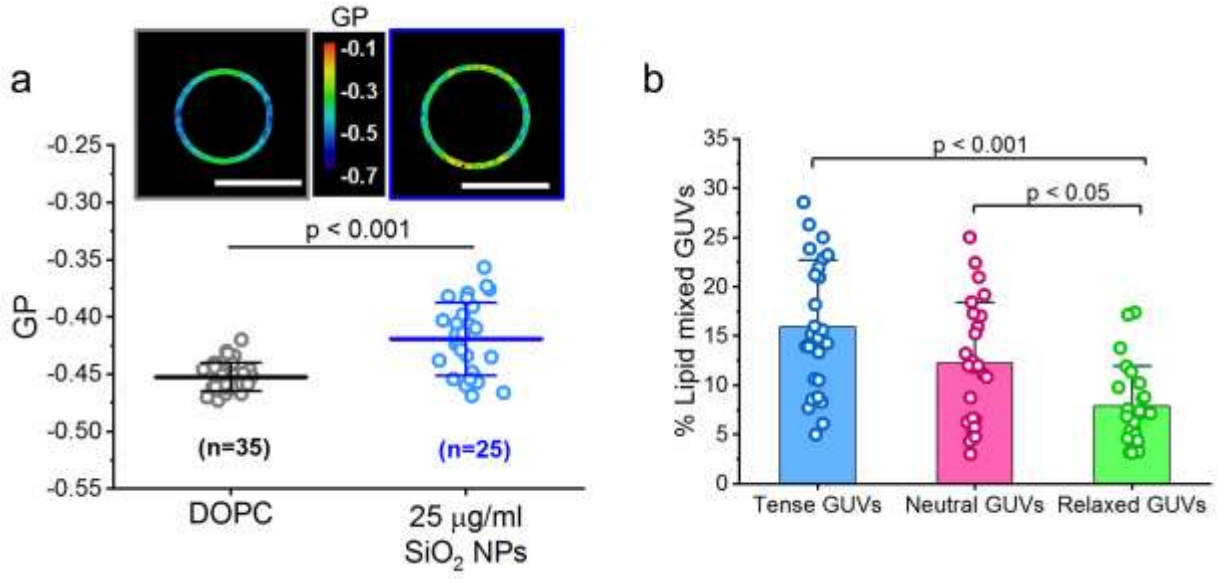

Figure 3. Effect of SiO_2 NPs on membrane order and impact of membrane tension on fusion efficiency of GUVs. a) Spectral imaging of DOPC GUVs labelled with Laurdan before and after incubation with 25 µg/ml SiO_2 NPs. GP images of a control GUV and a GUV after exposure to SiO_2 NPs. The graph shows that the distribution of average GP of the GUVs analysed increases slightly after incubation with 25 µg/ml SiO_2 NPs. Data are presented as mean ± standard deviation, circles indicate each individual measurement (number of individual datapoints indicated in the plot). b) Percentage of lipid mixed GUVs observed in confocal microscopy images depending on the membrane tension after incubation with 25 µg/ml SiO_2 NPs. The plot indicates a clear relationship between membrane tension and the proportion of GUVs undergoing fusion. The bars show the mean and the error bars the standard deviation. The overlayed circles represent the proportion of lipid mixed GUVs in each image analysed (Tense GUVs = 26 images; Neutral GUVs = 25 images; Relaxed GUVs = 24 images). The statistical significance in a and b was tested using a one-way ANOVA with a post-hoc Bonferroni test.

Silica nanoparticles induce fusion of GUVs *via* three different pathways

With the aim of getting a further mechanistic insight into the processes leading to membrane fusion, we perform additional real-time confocal microscopy experiments to record single fusion events between Rh-GUVs and DiO-GUVs. These experiments provide information about intermediate states as well as the kinetics of the fusion process by detecting the lipid mixing between GUV pairs.

First, we localise GUV pairs composed by one Rh-GUV and a DiO-GUV which show only red and green fluorescence, respectively. After SiO_2 NPs are added to the sample, we monitor changes in fluorescence intensity in each channel over time at the interface between vesicles and the more distal regions of each GUV. Our observations show that once SiO_2 NPs interact with a pair of GUVs, the vesicles adopt different intermediate states characterised by the degree of lipid mixing before their eventual fusion. The fusion process begins with a localised merging of the outer leaflets of the apposed GUVs as a result of high local curvature and lipid packing defects induced by the SiO_2 NPs. The resulting structure would be a fusion stalk where the inner monolayers of the neighbouring membranes form a bilayer in a small region where the GUVs are docked. The outer leaflets of the vesicle membranes thus reorganise themselves into a highly bent monolayer, which would be expected to begin to merge. [55] From this point, depending on the different intermediate states and morphological transitions that GUVs experience during a fusion event, we identify three main fusion pathways triggered by SiO_2 NPs.

Direct Full Fusion. In the first pathway, no or marginal intervesicular lipid exchange is observed before the GUVs fuse. The membrane breaks at one edge of the interface and the GUVs suddenly fuse. At the broken end, the lipids reorganise quicky forming highly dense and curved membrane structures, which vary between different fusion events, as seen in the enhanced fluorescence intensity of the dyes in that region of the membrane (Figures 4 and 2b). Immediately following fusion, the lipids from the original vesicles are observed to be not yet mixed,

and the new GUV shows two easily distinguishable hemispheres, one green and one red, which then mix rapidly in the new merged membrane (Figure 4, Supplementary Movie 4). The interaction of SiO_2 NPs with the membrane of the GUVs would induce membrane defects which generate a large elastic stress at the rim of the docking region. The stalk presumably originates at the edge of the boundary region but the persistent elastic stress would conceivably compel the membrane to break, forming a pore which would be anticipated to expand laterally along the perimeter of the docking zone. Consequently, the membrane region that was separating the individual GUVs would get trapped inside the new GUV and therefore reorganise to avoid exposure of hydrophobic lipid tails, forming an intraluminal vesicle (Figures 4 and 2b). The analysis of the size of the final GUVs compared to the initial GUVs shows that the volume of the final GUV is equivalent to the sum of the volume of the two initial GUVs (Figure S6).

A similar fusion mechanism was reported by Tanaka *et al.*, who observed that trivalent lanthanum ions (La^{3+}) induce the fusion of DOPC GUVs. [56] They propose that the outer monolayer of the membranes merge at one edge of the region, where membranes are in contact, and this destabilises the packing of the lipid tails that causes the breakage of the membrane, leading to fused GUVs with an intraluminal vesicle. Moreover, previous studies on vacuole fusion mediated by the SNARE complex have proposed that the formation of an intralumenal vesicle during the fusion occurs when the fusion pore forms at one point on the rim of the stalk and expands laterally along the perimeter entrapping a membrane fragment, which becomes an intraluminal vesicle. [57-58] In one of these studies, Mattie and colleagues showed that the expansion of the stalk into a hemifusion diaphragm inversely correlates with intralumenal fragment formation. [58]

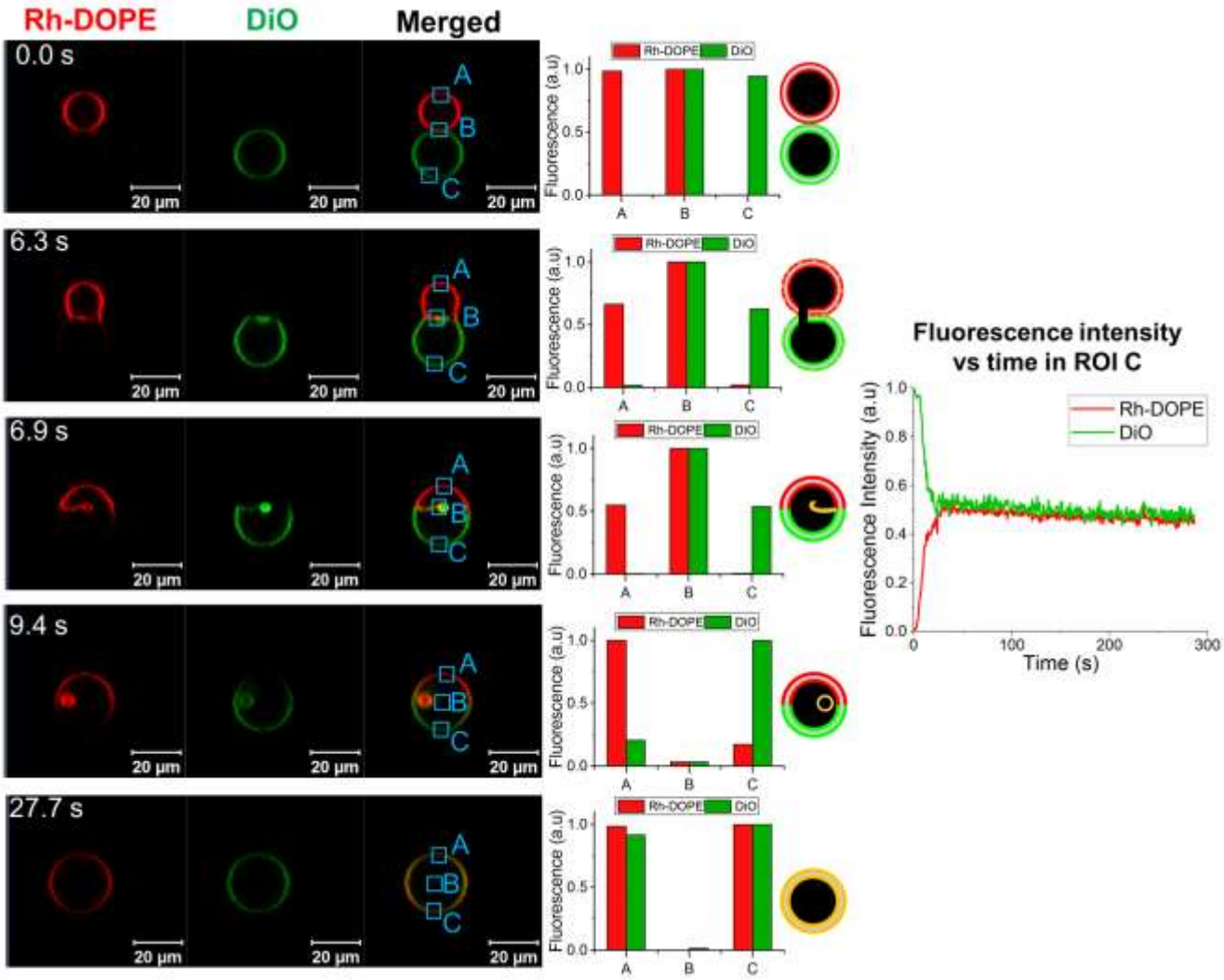

Figure 4. Fusion of GUVs *via* the sudden full fusion pathway. Confocal microscopy images show the state of the GUVs at particular stages of the process. DOPC GUVs are labelled with Rh-DOPE (red channel) and DiO (green channel). The bar plots show the fluorescence intensity of each fluorophore measured at the ROIs indicated by the blue boxes. Cartoons are schematic representations of the lipid mixing and topological transformations occurring in at that particular time point. The bar plots indicate that lipid mixing occurs after the GUVs fuse. The membrane boundary gets trapped in the final GUV and reorganise originating an intralumenal vesicle. The line plot displays the evolution of the fluorescence intensity in both channels over time at the ROI C.

Hemifusion – fusion. In this pathway, a gradual bidirectional exchange of lipids between the contacting GUVs is detected before the eventual fusion of the vesicles (Figure 5, Supplementary Movie 5). This second fusion pathway resembles the classic fusion model in which

the expansion of the stalk into a hemifusion diaphragm precedes the formation of the fusion pore [47, 59]. A hemifusion diaphragm is an intermediate state where the outer monolayers of the fusing GUVs are merged and the inner monolayers form a mixed bilayer at the contact region.

The hemifusion intermediate is detected by the presence of both dyes in the same GUV. [16, 60] Although the resolution of the confocal microscope does not allow us to see whether the dyes are located in the inner or the outer monolayer of the membrane, their fluorescence intensity is indicative of their presence in one or both leaflets of the bilayer. Before the fusion begins, the fluorescence intensity of Rh-DOPE is at its maximum in the Rh-GUV (bilayer intensity= 1; inner monolayer intensity=0.5; outer monolayer intensity=0.5), where it is present in both membrane leaflets. No Rh-DOPE fluorescence is observed in the initial DiO GUV. When the GUVs become hemifused, as only the lipids in the outer monolayer are mixed, the Rh-DOPE molecules in the outer monolayer of the Rh-GUV diffuse into the outer monolayer of the opposing GUV. Consequently, the dye gets diluted across the merged outer monolayer of the two GUVs. Assuming that the two vesicles have the same size, the relative intensity of Rh-DOPE in the Rh-GUV will now represent 75% of the initial intensity (bilayer intensity= 0.75; inner monolayer intensity=0.5; outer monolayer intensity=0.25) and the relative intensity of Rh-DOPE in the DiO-GUV will be 25% (bilayer intensity= 0.25; inner monolayer intensity=0; outer monolayer intensity=0.25). Therefore, if two GUVs of the same size become hemifused, we expect that the Rh-DOPE fluorescence intensity in the DiO GUV represent the 33% of its fluorescent intensity in the Rh GUV. Depending on the relative sizes of the GUVs this value can vary, but if only the outer monolayers are fused it is always expected to be lower than 50%. The same explanation applies to the fluorescence intensity of DiO but in the opposite direction.

The analysis of the fluorescence intensity in different regions of the GUVs indicate that the lipids of the outer leaflets mix completely before the GUVs fuse, as observed in Figure 5 (frame t=239.4 s). The enhanced fluorescence intensity displayed by both dyes at the GUV interface is

likely due to the existence of a small hemifusion stalk connecting the bilayers of the two GUVs. Images at longer times indicate a further level of lipid mixing, suggesting some extent of interleaflet lipid exchange. Eventually, a fusion pore opens and expands quickly through the hemifusion diaphragm and the GUVs fuse completing a classic hemifusion-fusion pathway. The newly formed GUV progressively adopts the spherical shape typical of vesicles and the lipids get homogeneously distributed across the membrane. In this case, the final GUV does not show the single intraluminal vesicle characteristic from the direct full fusion pathway.

The analysis of the GUVs size before and after fusion reveals a volume loss while the GUVs are hemifused (Figure S6). While the hemifusion is taking place, the GUVs slowly shrink and bright dots appear in their lumen, suggesting that lipids are being removed from the membrane by the SiO_2 NPs (Figure 5, Supplementary Movie 5). Cryo-EM studies have revealed that SiO_2 NPs completely wrapped by the membrane are internalised inside liposomes, showing a supported lipid bilayer coating removed from the membrane of the vesicle.[33, 61] A different investigation by Strobl *et al* showed that SiO_2 NPs are able to cross DOPC membranes and, during the process, they take small membrane sections with them, inducing the shrinkage of the GUV and a rise in its membrane tension. [42] This is very similar to what we observe in our experiments. Hence, the opening of the fusion pore would seemingly be driven by a further increase in membrane tension induced by SiO_2 NPs removing membrane surface area from the GUVs.

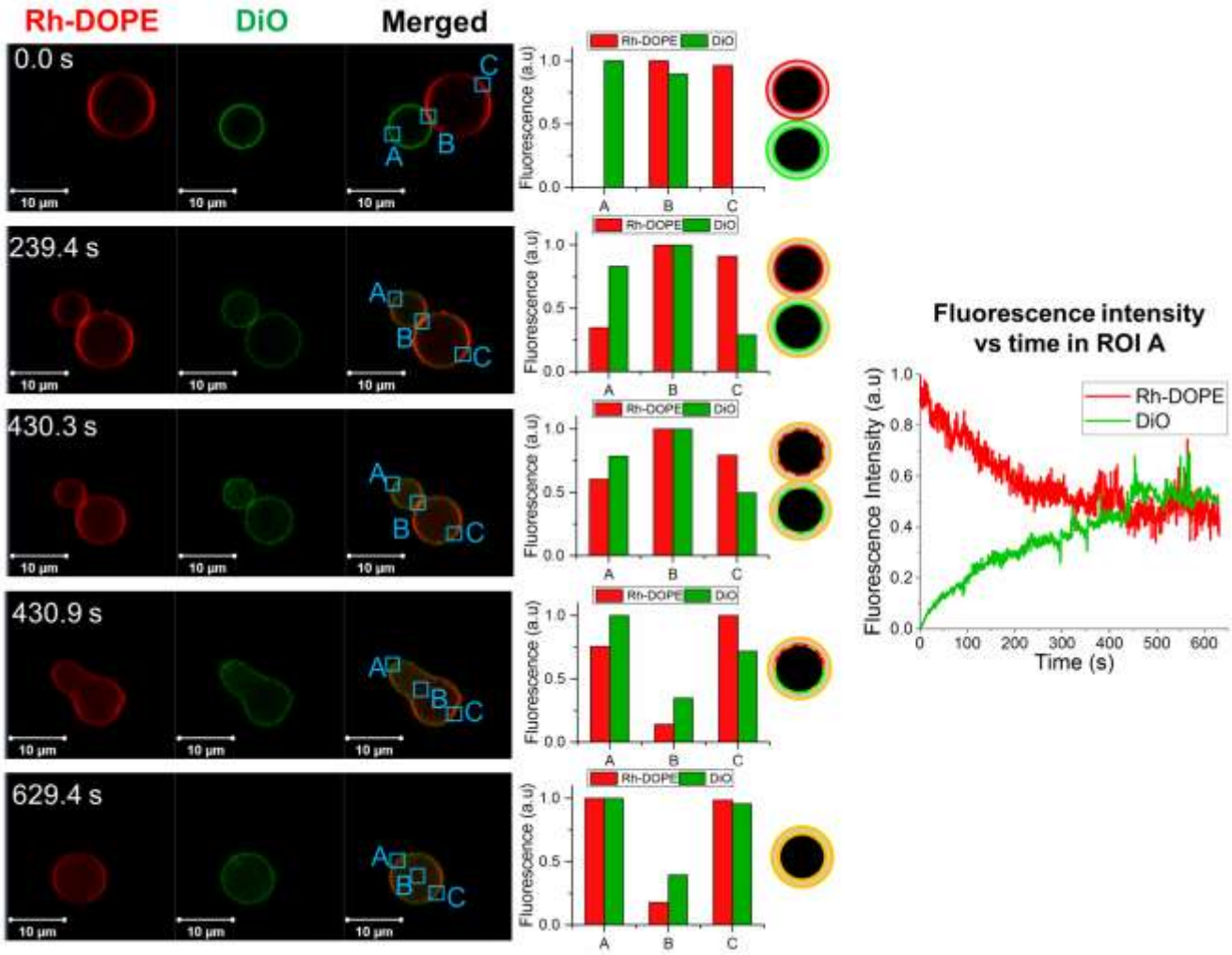

Figure 5. Fusion of GUVs *via* hemifusion-fusion pathway. Confocal microscopy images showing intermediate states of the fusion process. DOPC GUVs are labelled with Rh-DOPE (red channel) and DiO (green channel). The bar plots show the fluorescence intensity of each fluorophore measured at the ROIs indicated by the blue boxes. Cartoons are schematic interpretations of the data. The lipid mixing observed before the GUVs fuse indicates that a hemifusion intermediate has formed. Eventually the GUVs fuse. The fluorescence intensity observed in the lumen of the GUVs is likely to proceed from small patches of the membrane removed by the SiO_2 NPs. The line plot displays the evolution of the fluorescence intensity in both channels over time at the ROI A.

Gentle merging. Nevertheless, the fusion process cannot always be completed by the opening of a fusion pore at the hemifusion diaphragm. In these occasions, one of the GUVs is gradually absorbed by the other and their membranes fuse by a process that we have called gentle membrane merging (Figure 6, Supplementary Movie 6). Like in the previous pathway, the fluorescence intensity analysis indicates an initial lipid mixing just in the outer monolayers followed

by further lipid mixing in the inner monolayers. However, unlike the hemifusion-fusion pathway, during these events there is an apparent complete lipid mixing in both monolayers while the two GUVs are still separated. We hypothesise that the elastic stress at which the membranes are subjected would not be high enough to drive the opening of a large fusion pore at the hemifusion diaphragm. The tension at the hemifusion diaphragm is presumably stably maintained and the elastic stress could be totally relaxed at the rim of the hemifusion diaphragm by enhanced flip-flop rate and the formation of transient nanosized pores. As the lipid bilayers mix, one of the apposed GUVs gets progressively smaller and its membrane is transferred to the neighbouring vesicle, which consequently grows until the shrinking GUV is completely engulfed and only one GUV with a fully mix membrane survives. The result from these events is then a GUV formed by a mixture of the membranes from the two initial GUVs and whose volume equals the sum of the volumes of the initial vesicles (Figure S6).

The precise mechanism for gentle merging is unclear. Here we aim to propose a plausible explanation where, once the GUVs become hemifused and before the fusion pore can open, there is a stochastic disruption in stability of one of the vesicles that allows the transfer of its membrane to the apposed GUV. The growth of one GUV by absorbing the membrane of the apposing GUV might then be driven by its Laplace pressure. However, from our current observations, there is insufficient experimental evidence to claim a definitive mechanism that explains the gentle membrane merging events.

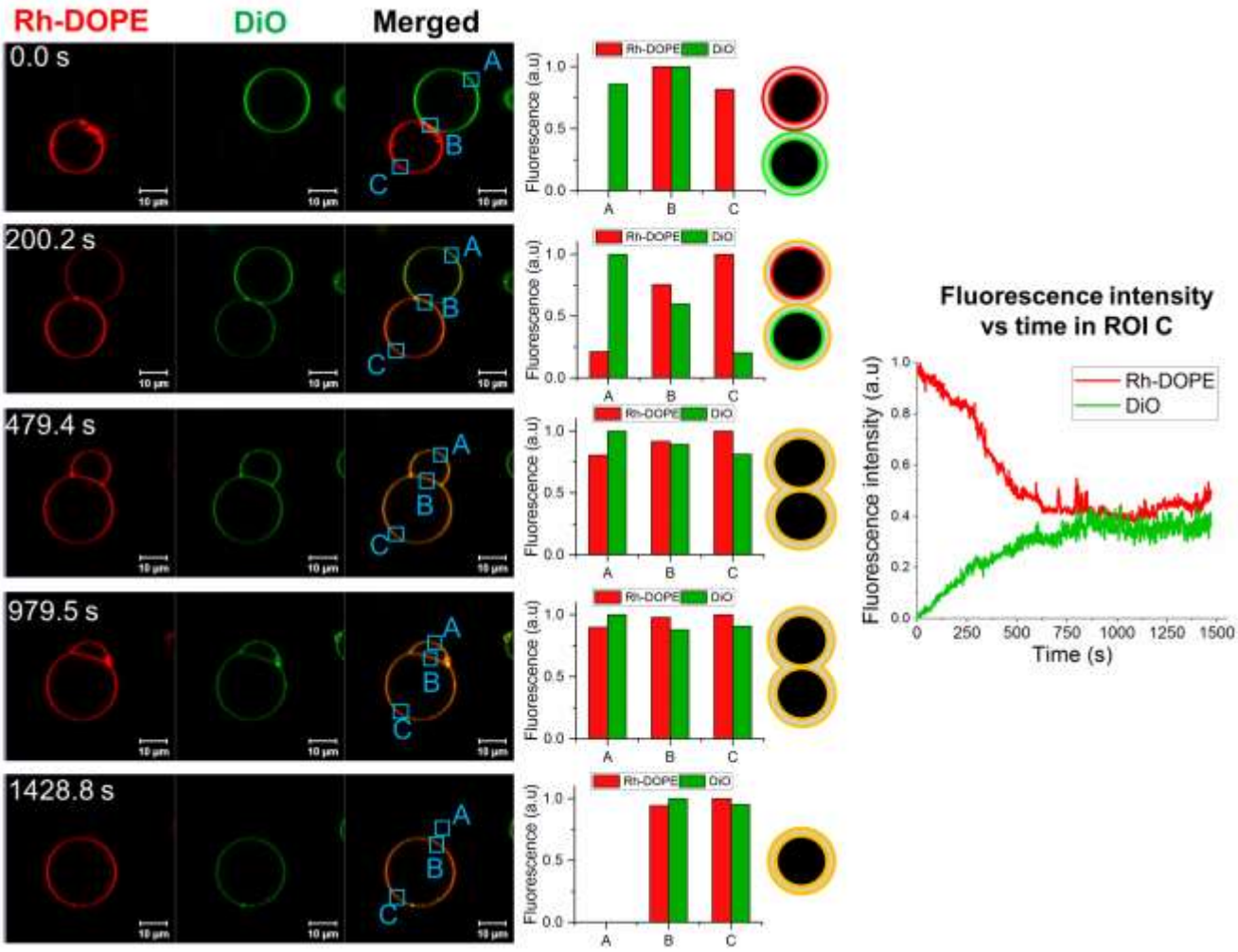

Figure 6. Fusion of GUVs *via* gentle merging pathway. Confocal microscopy images show the state of the GUVs at different stages of the process. The DOPC GUVs are labelled with Rh-DOPE (red channel) and DiO (green channel). The bar plots show the fluorescence intensity of each fluorophore measured at the ROIs indicated by the blue boxes. Cartoons are schematic interpretations of lipid mixing membrane configuration state at the stage of the process shown in the micrographs. The lipid mixing observed before the GUVs fuse indicates that a hemifusion intermediate has formed. One of the GUVs gradually shrinks and the other GUV grows consequently. At the same time their membranes merge gently until forming a single GUV with a mixed membrane. The line plot displays the evolution of the fluorescence intensity in both channels over time at the ROI C.

The rate of lipid mixing is slower in fusion pathways involving hemifusion intermediates

Further analysis of the confocal time series allows quantification of the rate of lipid mixing in the different fusion pathways. For this analysis, we measure the increase in fluorescence intensity over time from the moment when one of the dyes begin to migrate into its neighbouring vesicle. The increase of fluorescence intensity over time was well described by an exponential decay function. The time constant obtained from the empirical exponential fitting was used to calculate the rate of lipid mixing along the membrane surface.

The results summarised in Figure 7 show a much slower lipid mixing rate when the fusion pathway involves the formation of a hemifusion diaphragm. The lipid mixing rate calculated from the direct full fusion events ($3.22 \pm 0.60\ \mu m^2\ s^{-1}$) is consistent with literature values for the lateral diffusion coefficient of DOPC [34, 62], therefore in this pathway the lipid mixing is driven solely by the lateral diffusion of lipids once the vesicles have fused.

In contrast, the lipid mixing rates estimated for the other two fusion pathways are considerably slower than DOPC lateral diffusion, with values of $0.33 \pm 0.36\ \mu m^2\ s^{-1}$ for the hemifusion-fusion pathway and $0.48 \pm 0.24\ \mu m^2\ s^{-1}$ for the gentle merging. Similar slow diffusion of lipids has been reported previously in protein-free and SNARE-mediated hemifused GUVs. [19, 60] We observe that full bilayer mixing can be reached while the GUVs are hemifused. This bilayer mixing may result from enhanced lipid flip-flop between the membrane leaflets which considerably reduces the rate of lipid mixing compared to lateral diffusion alone. The formation of a stable hemifusion diaphragm implies that the surface area of the inner leaflets of the membranes must be larger than that of outer monolayers. This requires the transport of lipids from the outer leaflet to the inner leaflet *via* flip-flop. The lipid flip-flop would be expected to be particularly enhanced at the rim of the hemifusion diaphragm. In this region, the significant negative curvature of the

membrane likely generates a mechanical stress different in each monolayer and the membranes becomes highly unstable. The differential mechanical stress derived from increased membrane curvature as well as local membrane deformations are known to significantly increase the rate of interleaflet lipid transport. [63-64] Moreover, molecular dynamics simulations have shown that lipid flip-flop is a preferential mechanism to reduce the instability at the junction site of three bilayers and maintain a metastable hemifusion diaphragm. [65]

Another potential contribution to bilayer lipid mixing involves the formation of transient nanoscopic pores in the membrane, which allows short-lifetime pulses of lipid transfer between monolayers. Such interleaflet lipid exchange would relax the stress in the membrane by the net removal of lipids from the compressed outer monolayer to the expanded regions of the inner leaflets during the bidirectional diffusional exchange of lipids across the open pore.

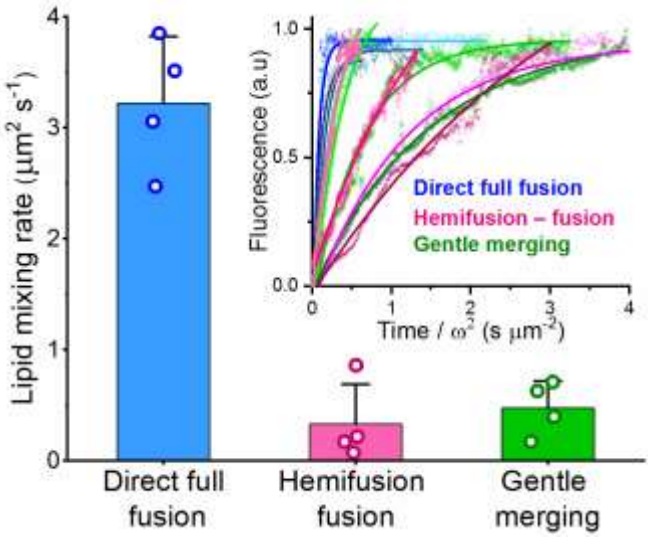

Figure 7. Rate of lipid mixing during each fusion pathway. The calculated average lipid mixing rate for the fusion events *via* direct full fusion is 3.22 ± 0.60 $\mu m^2 s^{-1}$ whereas the hemifusion-fusion pathway and the gentle merging show reduced lipid mixing rates, 0.33 ± 0.36 $\mu m^2 s^{-1}$ and 0.48 ± 0.24 $\mu m^2 s^{-1}$, respectively (The bar plot show the mean and standard deviation with the individual datapoints overlayed). The inset plot shows the normalised fluorescence intensity of the dye when it begins to colonise a membrane where it was not present initially as a function of time per unit area. The curves of individual events were fitted using an exponential function (see methods) to estimate the rate of lipid diffusion.

CONCLUSIONS

In this work, we introduce a protein-free membrane fusion platform based on the ability of 30 nm SiO_2 NPs to trigger membrane curvature and tension that mimics the physicochemical effects of natural protein complexes for membrane fusion. Initial FRET experiments performed in bulk LUV populations show a significant increase in intervesicular lipid mixing dependent on the concentration of SiO_2 NPs in solution. The fusogenic activity of SiO_2 NPs is confirmed by direct imaging of GUVs using confocal microscopy. To the best of our knowledge, this is the first time that membrane fusion induced by passive nanoparticle-membrane interactions is predicted and demonstrated. Where nanoparticles have been used to trigger membrane fusion in the past, this has been due to secondary effects where, for example, electromagnetic fields have been used to stimulate local heating by the nanoparticles. [22-24] This finding fits within the classical theoretical framework for nanoparticle membrane adhesion and wrapping but finds its novelty in probing the experimentally unexplored cross-over region between the well-known membrane adsorption and membrane wrapping dominated regimes. At this cross-over, the adhesion energy of the nanoparticle exactly balances the bending energy of the membrane to wrap a particle of that specific size. Strikingly, a new phenomenon of NP-induced membrane fusion is observed at the intersection between these two previously reported regimes.

Figure 8 summarises our proposed nanoscale molecular mechanisms that occur as SiO_2 NPs induce the contact and fusion of two membranes. Based on our observations, we propose a scenario where membrane tension is the principal driving force of the fusion events. This view agrees with many studies, including theoretical models, [47, 66] simulations [50-51, 67] and experimental investigations. [52, 68] In our system, the fusion process starts when SiO_2 NPs in suspension interact with closely localised GUVs. This interaction is likely to favour the close approach between the membranes of two GUVs by inducing local changes in membrane curvature. Molecular simulations have shown that any protein complex located between two opposing membranes

generates a local membrane curvature that promotes the close apposition of the opposing leaflets needed to begin the fusion process. [69] In addition, we have seen that the SiO_2 NPs affect the lipid packing within the membrane. The negative surface charge of SiO_2 NPs is predicted to produce a reorientation of the headgroup dipole of DOPC lipids generating an electrostatic condensation of the area per lipid in the outer membrane leaflet, which would generate a considerable increase in membrane tension. [70]

The fusogenic activity of SiO_2 NPs relies on its capacity to generate increased membrane tension, high enough to overcome the different energy barriers during the fusion process. The energy required to initiate the fusion process and form the fusion stalk has been estimated to be in the range of 20-35 k_BT.[71-72] The increase in membrane tension generates elastic stress which, along with high local membrane curvature and lipid packing defects, would result in highly energetically unfavourable exposure of hydrophobic membrane regions to the aqueous environment. The elastic stress is likely released by the reorganisation of the membranes in the boundary between the GUVs so the exposed hydrophobic region of one membrane matches the hydrophobic region of the inner leaflet of the adjacent membrane. [16] This leads to the formation of the fusion stalk where the outer monolayers of the membranes start merging.

After the stalk is formed, GUVs can follow three different observed pathways that lead to membrane fusion: i) direct full fusion, ii) hemifusion-fusion and iii) gentle merging. The fastest but more energetically demanding process is the direct full fusion. The opening of the fusion pore directly from the stalk implies an energy cost of around 100 k_BT.[71] Hence a significant increase in membrane tension would be needed for the membranes to fully fuse immediately after the stalk formation. Such high energetic cost implies that the membrane tension acquired is not always sufficient to trigger this pathway. However instead of aborting the process, the system finds an alternative route, the hemifusion intermediate, which is slower but requires less energy. The energy barrier for the expansion of the stalk into a hemifusion diaphragm can vary between 15

and 35 k_BT depending on the lipid composition, the membrane tension and the spontaneous curvature [71, 73]. At this point, a further increase of the membrane tension could drive the opening and expansion of the fusion pore at the hemifusion diaphragm to complete the hemifusion-fusion pathway. Again, if the energy needed for the opening and expansion of a fusion pore at the hemifusion diaphragm (35-40 k_BT)[71] cannot be overcome, the process is finished *via* gentle membrane merging. At this lower tension, the probability of a stochastic disruption of the membrane of one vesicle occurring before a full fusion pore opens increases. Once one vesicle is disrupted, it begins to shrink while the other vesicle grows and takes up lipids from the disrupted vesicle. This process is potentially driven by the Laplace pressure of the growing vesicle.

The effect of membrane tension in the fusion efficiency was evaluated in LUVs and GUVs using FRET and confocal microscopy, respectively. Our results show a higher proportion of vesicles fused or undergoing fusion when the tension of their membranes was osmotically increased and vice versa. Unfortunately, our experimental approach does not allow to quantify the proportion of fusion events taking place through each different pathway, so different strategies might be considered in the future to overcome this limitation and get more information about biophysical parameters influencing which fusion pathway is going to be followed.

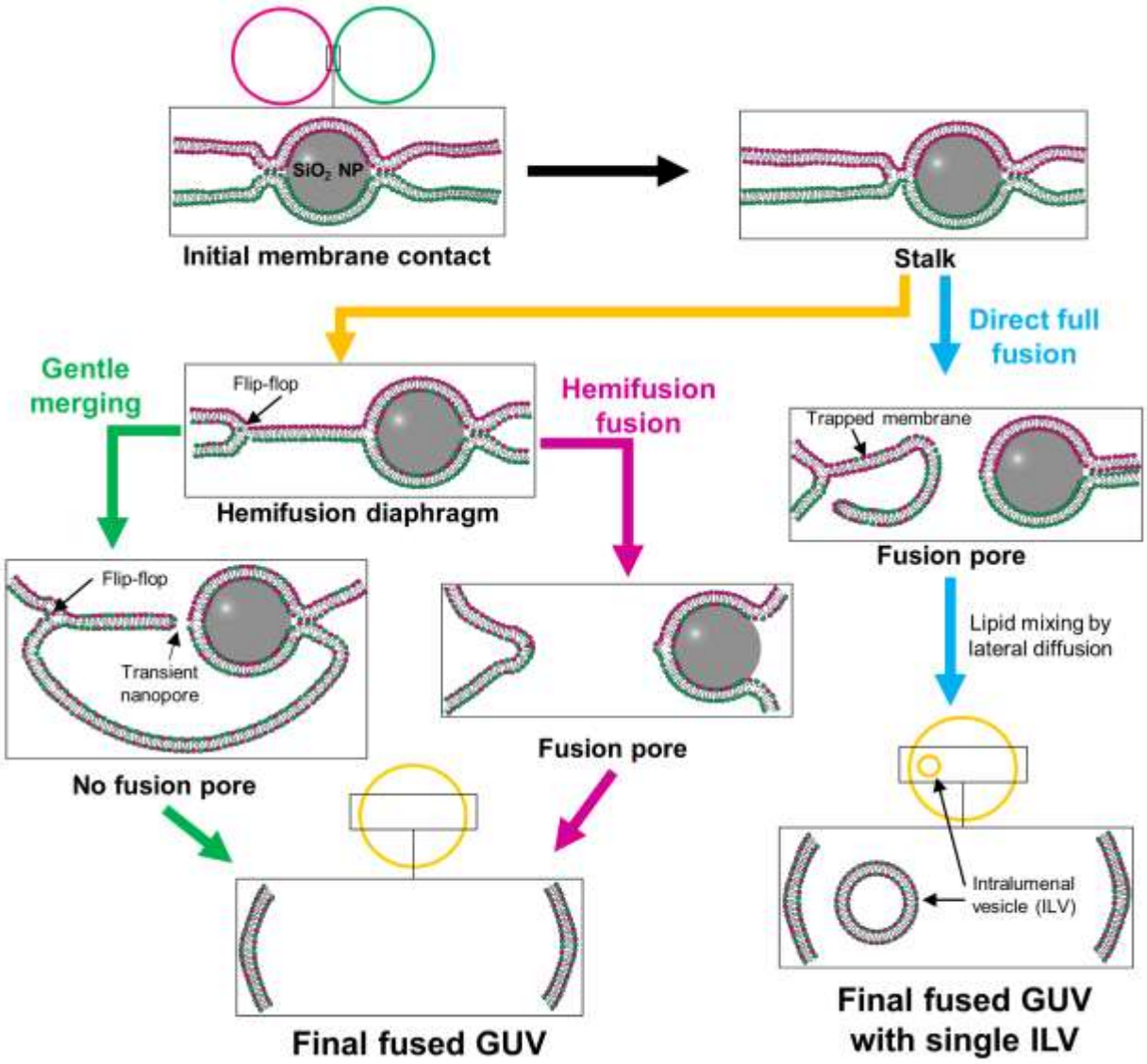

Figure 8. Schematic representation of membrane transitions occurring at the docking region during fusion events triggered by SiO_2 NPs. The SiO_2 NPs facilitate the initial contact between two membranes and induce high local curvature, increased tension and lipid packing defects. This promotes the formation of a stalk. At this point, a fusion pore can form directly from the stalk leading to a sudden full fusion of the GUVs. After the GUVs fuse the lipids in the membrane mix *via* lateral diffusion and the membrane previously placed at the boundary is trapped in the lumen and forms an intralumenal vesicle (Sudden full fusion pathway). The stalk can also expand into a hemifusion diaphragm stabilised by enhanced lipid flip-flop at its rim. If a fusion pore opens at the hemifusion diaphragm the fusion process is completed (Hemifusion-fusion pathway). However, if this does not happen the hemifusion diaphragm persists stabilised by flip-flop and transient nanopores. In this case, one of the GUVs is gradually absorbed by the other one and their membranes gently merge (Gentle membrane merging pathway).

Since the effect that SiO_2 NPs of a given size produce in lipid membranes depends on the balance between adhesive forces and the elastic properties of the membrane, changes in the solution environment (such as ionic strength, pH, temperature), SiO_2 NPs surface functionalisation and membrane composition might affect the fusogenic activity of 30 nm SiO_2 NPs. Modifications of such parameters have not yet been investigated, but it is possible that new experimental conditions might require changing the SiO_2 NP size to maintain the right balance between adhesion and bending energies needed to obtain fusogenic activity. For instance, protein coronas have been reported to weaken the interaction between different types of NPs, including SiO_2 NPs, and biological membranes and increase the hydrodynamic size of the particles, so the fusogenic activity of 30 nm SiO_2 NPs might be inhibited by a protein corona. On the other hand, the NP functionalisation with amphiphilic molecules such as oleic acid and alkanethiol, has been seen to promote fusogenic activity of magnetite (Fe_3O_4) nanoparticles and gold, respectively. [26, 74]

Beyond the balance of adhesion and bending energies, the size of the nanoparticle may also be important in obtaining fusogenic activity. A previous study by Dinsmore and collaborators aimed to present a unified picture of vesicle topological transitions induced by nanoparticles by investigating the interaction of charged nanoparticles with oppositely charged vesicle membranes. [54] In that work the authors used smaller nanoparticles than the LUDOX TM-50 nanoparticles in this current study, some of which had a radius (a) similar to the thickness of the lipid bilayer. Membrane rupture and GUV destruction were observed for $wa^2/\kappa > 0.6$ and membrane fusion was not reported. [54] Notably, we propose that $wa^2/\kappa \sim 2$ is required for membrane fusion, a regime that was inaccessible in the study by Dinsmore and collaborators. This is suggestive that a minimum nanoparticle size may be necessary to observe fusion such that the radius of curvature of the nanoparticle is not so great that the membrane ruptures during partial wrapping. Further studies are however needed to determine the width of the range of the wa^2/κ parameter and SiO_2

NPs size where membrane fusion is observed. In addition, this model is only valid for spherical particles with homogeneous surface curvature, while non-spherical particles show inhomogeneous surface curvature and therefore can induce different membrane deformations depending on their orientation when they contact with the membrane. [75]

Our results offer the prospect of using SiO_2 NPs as a nanotechnological tool in synthetic biology to create more complex model membrane systems, which better mimic the properties of cell membranes. These systems would mix the cargo of two vesicles and trigger chemical reactions. These NPs are inexpensive to produce, can remain colloidally stable in solution for long periods of time and can easily be tuned to boost particular advantageous properties.

A current major challenge in the study of membrane remodelling processes is understanding the role that Gaussian curvature plays in them. The experimental investigation of Gaussian curvature is very challenging and requires membrane systems whose topology can be tightly controlled. [69] Within this context engineered nanoparticles and vertical nanostructures are interesting strategies for precise control of membrane topology. [76-77] The fact that the same fusogen can induce membrane fusion *via* different pathways represents an advantage for the study of membrane fusion mechanisms because it implies that by changing particular conditions (membrane composition, vesicle shape, ionic strength of the medium, presence of macromolecules and divalent cations such as Ca^{2+}, *etc.*) the system could potentially be tuned to favour a specific fusion pathway over the others and give information about the influence of specific parameters, such as membrane curvature and tension, in the fusion process. Also, the surface of the SiO_2 NPs can be functionalised to increase or decrease their affinity for the membrane. Therefore, SiO_2 NPs are a promising synthetic biology tool for triggering membrane fusion in a broad range of experimental scenarios.

METHODS

Materials

DOPC (1,2-dioleoyl-sn-glycero-3-phosphocholine), Rh-DOPE (1,2-dioleoyl-sn-glycero-3-phosphoethanolamine-N-(lissamine rhodamine B sulfonyl) (ammonium salt)), and NBD-DOPE (1,2-dioleoyl-sn-glycero-3-phosphoethanolamine-N-(7-nitro-2-1, 3-benzoxadiazol-4-yl) (ammonium salt)) were purchased from Avanti Polar Lipids Inc. (Alabaster, Alabama, USA). Colloidal SiO_2 NPs LUDOX TM-50 (50 wt. % suspension in H_2O), Tetramethylrhodamine isothiocyanate (TRICT)-Dextran 70 kDa, indium tin oxide (ITO) coated glass slides (surface resistivity 8–12 V sq-1), HEPES (4-(2-hydroxyethyl)-1-piperazineethanesulfonic acid), sodium chloride (NaCl), sucrose ($C_{12}H_{22}O_{11}$), and bovine serum albumin (BSA) were obtained from Sigma-Aldrich Co. (Gillingham, UK). DiO (3,3'-Dioctadecyloxacarbocyanine Perchlorate) and DiD (1,1'-Dioctadecyl-3,3,3',3'-Tetramethylindodicarbocyanine, 4-Chlorobenzenesulfonate Salt) were purchased from ThermoFisher Scientific Ltd. (Loughborough, Leicestershire, UK). Microscope µ-slide 8 well glass bottom chambers (Ibidi GmbH) were purchased from Thistle Scientific Ltd (Glasgow, UK).

Dynamic Light Scattering

The hydrodynamic diameter and colloidal stability of SiO_2 NPs was measured by dynamic light scattering (DLS) using a Malvern Zetasizer Nano ZSP (Malvern Panalytical, Malvern, UK) at a fixed 173° back-scattering angle. SiO_2 NPs were incubated in buffer (20 mM HEPES, 150 mM NaCl, pH 7.4) for 1 hour and then measured three times to obtain the hydrodynamic diameter. The same sample was measured again after 24 h and 48 h to evaluate the colloidal stability of the NPs over time. The same instrument was used to measure the ζ potential of the SiO_2 NPs *via* dynamic electrophoretic light scattering analysis (DELSA). In this case the scattering angle was 17° and the ζ potential was estimated from the measured electrophoretic mobility of the NPs using

the Smoluchowski approximation. DLS and DELSA results were processed using the Malvern Zetasizer software.

DLS was also employed to determine the hydrodynamic size of DOPC LUVs before and after incubation with SiO_2 NPs. The LUVs were diluted in buffer (20 mM HEPES, 150 mM NaCl, pH 7.4) to a final lipid concentration of 100 µM. The LUVs suspension was incubated for 30 minutes with 30 µg/ml and 100 µg/ml of SiO_2 NPs, and a control sample without SiO_2 NPs was used as control.

Transmission electron microscopy

Transmission electron microscopy (TEM) was conducted on an FEI Tecnai TF20 field emission gun (FEG) TEM operating at 200 kV and fitted with a Gatan Orius SC600A CCD camera. For TEM analysis, a drop of the dispersed sample was placed on a continuous carbon coated copper grid (EM Resolutions, Sheffield, UK). After being left to dry, this was transferred to the TEM. More than 1000 nanoparticles were analysed using Fiji to calculate the size distribution of SiO_2 NPs.

Preparation of large unilamellar vesicles

Large unilamellar vesicles (LUVs) were prepared by the extrusion method. The desired lipids were mixed at 25 mM in chloroform to get a final volume of 200 µl. The organic solvent was evaporated under high vacuum overnight to get a dry lipid thin film which was then rehydrated with 500 µl of buffer (20 mM HEPES, 150 mM NaCl, pH 7.4). The resulting suspension was subjected to 10 freeze-thaw cycles and then extruded 11 times by passing through a 400 nm pore size polycarbonate membrane (Whatman International Ltd., Maidstone, UK) using a LiposoFast extruder (Avestin Inc.) to obtain a homogeneous population of LUVs.

Lipid mixing assay

The intervesicular lipid mixing was determined by measuring the Förster Resonance Energy Transfer (FRET) between NBD and rhodamine (Rh). For these experiments, we prepared non-labelled DOPC LUVs and DOPC LUVs labelled with 0.25 mol% NBD-DOPE and 0.25 mol% Rh-DOPE. The two sets of LUVs were mixed in a 1:4 ratio (100 µM) and incubated during 30 minutes with SiO_2 NPs at 3 µg/ml, 10 µg/ml, 30 µg/ml and 100 µg/ml. In addition, samples of LUVs non-exposed to SiO_2 NPs (0 µg/ml) were used as negative control and samples of DOPC LUVs labelled with 0.05 mol% NBD-DOPE and 0.05 mol% Rh-DOPE were used as full lipid mixing control. The fluorescence intensity of the samples was measured between 500 nm and 650 nm with a FluoroMax-Plus spectrofluorometer (Horiba Scientific), using the excitation wavelength of NBD (460 nm). The maximum fluorescence intensity of NBD (I_{NBD} at 530 nm) and Rh (I_{Rh} at 590 nm) were used to calculate the FRET ratio (R) of each sample as $R = I_{Rh} / I_{NBD}$. The percentage of lipid mixing was then calculated by normalising the FRET ratios of each sample (R_n) between the baseline samples of LUVs untreated with SiO_2 NPs (R_0) and the full lipid mixing controls (R_{full}):

$$\% \, Lipid \, mixing = \frac{R_n - R_0}{R_{full} - R_0} \, x \, 100$$

Moreover, we also measured the maximum fluorescence intensity at 530 nm of DOPC LUVs labelled only with 0.25 mol% NBD-DOPE. The values of the maximum fluorescence intensity of NBD (donor) when the acceptor Rh is present (I_{DA}) and absent (I_D) was used to calculate the FRET efficiency (E) using: $E = 1 - (I_{DA} / I_D)$.

Electroformation of giant unilamellar vesicles

Giant unilamellar vesicles (GUVs) were prepared by the electroformation method from 0.7 mM DOPC. Depending on the experiment, the GUVs were labelled with 0.5 mol% Rh-DOPE (Rh-GUVs), 1 mol% DiO (DiO-GUVs), 1 mol% DiD or 0.5 mol% Laurdan, by adding the correspondent dye to the DOPC solution in chloroform. For the electroformation, 15 µL of lipid solution were

deposited on the conductive side of indium-tin oxide (ITO) coated glass slides and then dried under a nitrogen stream to form a thin film. Then, the electroformation chamber was assembled using two ITO slides, each in contact with a copper tape, separated by a 1.6 mm Teflon spacer. The chamber was filled with 300 mM sucrose solution (300 mOsm/kg) and connected to a function generator to apply an AC field. The frequency was set at 10 Hz and the voltage was gradually increased from 1 V peak-to-peak (V_{pp}) to 5 V_{pp} over 15 minutes and maintained at 5 V_{pp} and 10 Hz for two hours. Finally, the frequency was gradually reduced to 0.1 Hz over 10 minutes to facilitate the closure and detachment of GUVs from the slide. After electroformation, the GUVs were diluted (1:5) with isotonic buffer (20 mM HEPES, 150 mM NaCl, pH 7.4, 300 mOsm/kg) unless otherwise specified. For experiments where the membrane tension of the GUVs needs to be osmotically modified, the osmolality of the buffer in which the GUVs were diluted after electroformation was reduced or increased by 10 mOsm/kg to obtain tense GUVs or relaxed GUVs, respectively. [62, 78] The osmolality of the buffers was measured with a freezing point depression Advanced Instruments 3320 osmometer.

To prepare GUVs loaded with fluorescent dextran, we added 1 mg/ml of TRITC-dextran 70 kDa to the sucrose solution used to rehydrate the lipid film in the electroformation chamber. The electroformation was carried out as explained above. After the electroformation, unencapsulated fluorescent dextran was removed from the medium by centrifugation washing protocol. [79] 200 µl of GUVs were diluted with 800 µl of buffer (20 mM HEPES, 150 mM NaCl, pH 7.4) and then centrifuged at 100*x g* for 3 minutes. The supernatant containing free dextran was removed and the sedimented GUV are resuspended with 800 µl of fresh buffer. The process was repeated 2 more times and in the final round the GUVs are resuspended to a final volume of 600 µl.

Confocal microscopy

The GUV-fusion experiments were performed at room temperature on a Zeiss LSM-880 inverted laser scanning confocal microscope with a Plan-Apochromat 40x/1.4 Oil DIC M27

objective lens (NA = 1.4). The glass surfaces of the 8-well microscope chamber slides were treated with 5% BSA solution in mili-Q water for 10 minutes and then rinsed with mili-Q water and dried under a nitrogen stream to prevent GUVs from adhering and rupturing onto the glass. 200 µl of GUVs were deposited into a well of the microscope slide and, once the GUVs were sunk in the bottom of the well, 25 µg/ml SiO_2 NPs were carefully added to the sample. All GUVs observed in this study were between 8 µm and 30 µm (diameter of equatorial plane). DiO and Rh were excited with a 488 nm argon laser and a 561 nm diode pumped solid state (DPSS) laser, respectively. The emission of DiO was recorded between 493 nm and 553 nm and the emission of Rh between 566 nm and 630 nm. The excitation and emission of TRITC dextran was the same as for Rh. DiD was excited at 633 nm with a HeNe laser and its fluorescence emission was detected between 640 nm and 750 nm.

Laurdan spectral imaging

GUVs labelled with 0.5 mol% Laurdan were prepared by electroformation. The spectral imaging was acquired using the lambda mode of the Zeiss LSM880 confocal microscope. Laurdan was excited at 405 nm and the fluorescence detection range was set between 410 nm and 550 nm with a spectral step of 8.9 nm per channel. Snapshots of Laurdan labelled GUVs were acquired before and after exposure to 25 µg/ml SiO_2 NPs. If the lipid packing within the membrane increases, the maximum fluorescence of Laurdan experience a blue shift from 490 nm (I_{490}) to 440 nm (I_{440}). The images were analysed with a Fiji plugin developed by Sezgin *et al*, [80] setting 440 nm and 490 nm as maximum emission wavelengths to calculate the GP values using the following equation:

$$GP = \frac{I_{440} - I_{490}}{I_{440} + I_{490}}$$

Estimation of proportion of lipid mixed GUVs

The proportion of GUVs undergoing fusion in the samples was quantified by taking confocal microscopy tile scans of large sample areas containing a 1:1 (vol:vol) mixture of Rh-GUVs and DiO-GUVs, after incubation with 25 µg/ml SiO_2 NPs for 30 minutes. GUVs with both dyes colocalised in the membrane were counted as lipid mixed GUVs. The number of lipid mixed GUVs in each tile image was counted manually and reported as the proportion respect the total number of GUVs. These experiments were repeated for tense GUVs, neutral GUVs (in isotonic buffer) and relaxed GUVs to assess the influence of the membrane tension in the fusion process.

Detection of fusion intermediate states and estimation of lipid mixing rate

A mixture of Rh-GUVs and DiO-GUVs (1:1; vol:vol) was exposed to 25 µg/ml SiO_2 NPs. Confocal microscopy time series were acquired to follow fusion processes taking place between pairs of oppositely labelled GUVs over time. Images were analysed with Fiji to measure the fluorescence intensity of each fluorophore in different regions of interest of the GUVs membranes.

For the estimation of the lipid mixing rate, we monitored the fluorescence increase over time of one of the dyes when it invades the GUV initially labelled with the other fluorophore. For the data analysis, our approach is based on a methodology commonly used in fluorescence recovery after photobleaching (FRAP) studies.[60, 81-83] First, the fluorescence intensity was normalised to the maximum intensity reached after fusion. The data was then fitted to an exponential function $f(x) = A(1-exp(-t/\tau))$ where, A is the change in fluorescence, t is the time passed since the lipids begin to mix and τ is the time constant. The rate of lipid mixing is calculated as the diffusion coefficient (D): $D=\omega^2/4\tau$, where ω is the radius of a circle with a surface area equivalent to the GUV analysed. The analysis of the images was performed with Fiji and the data was fitted using Origin Pro.

Supporting information

TEM and DLS characterisation of SiO_2 NPs. Example of FRET spectrum and FRET ratio and efficiency. Table of DLS data of individual LUVs samples. Examples of Laurdan GP maps of DOPC GUVs before and after exposure to SiO_2 NPs. Influence of membrane tension in fusion efficiency of LUVs measured by FRET. Ratio of volume change of GUVs after fusion though different pathways. Confocal microscopy movies of GUV fusion.

Data availability

The datasets and movies that support the findings of this study are available in the White Rose repository with the identifier (https://doi.org/10.5518/929).

ACKNOWLEDGEMENTS

The authors thank Dr Nicole Hondow (School of Chemical and Process Engineering, University of Leeds) for the acquisition of the TEM images of the nanoparticles. PAB acknowledges support from a UK Engineering and Physical Sciences Research Council (EPSRC) grant (EP/M027929/1). MAP is grateful to the University of Leeds for funding through the Lowson Scholarship.

REFERENCES

1. Martens, S.; McMahon, H. T., Mechanisms of Membrane Fusion: Disparate Players and Common Principles. *Nature Reviews Molecular Cell Biology* **2008,** *9* (7), 543-556.

2. Sudhof, T. C.; Rothman, J. E., Membrane Fusion: Grappling with SNARE and SM Proteins. *Science* **2009,** *323* (5913), 474-477.

3. Gopfrich, K.; Platzman, I.; Spatz, J. P., Mastering Complexity: Towards Bottom-up Construction of Multifunctional Eukaryotic Synthetic Cells. *Trends in Biotechnology* **2018,** *36* (9), 938-951.

4. Kretschmer, S.; Ganzinger, K. A.; Franquelim, H. G.; Schwille, P., Synthetic Cell Division via Membrane-Transforming Molecular Assemblies. *Bmc Biology* **2019,** *17*, 47.

5. Walde, P.; Cosentino, K.; Engel, H.; Stano, P., Giant Vesicles: Preparations and Applications. *Chembiochem* **2010,** *11* (7), 848-865.

6. Fenz, S. F.; Sengupta, K., Giant Vesicles as Cell Models. *Integrative Biology* **2012,** *4* (9), 982-995.

7. Elani, Y.; Law, R. V.; Ces, O., Vesicle-Based Artificial Cells as Chemical Microreactors with Spatially Segregated Reaction Pathways. *Nature Communications* **2014,** *5*, 5305.

8. Hindley, J. W.; Elani, Y.; McGilvery, C. M.; Ali, S.; Bevan, C. L.; Law, R. V.; Ces, O., Light-Triggered Enzymatic Reactions in Nested Vesicle Reactors. *Nature Communications* **2018,** *9*, 1093.

9. Blanken, D.; Foschepoth, D.; Serrao, A. C.; Danelon, C., Genetically controlled membrane synthesis in liposomes. *Nature communications* **2020,** *11* (1), 4317-4317.

10. Berhanu, S.; Ueda, T.; Kuruma, Y., Artificial Photosynthetic Cell Producing Energy for Protein Synthesis. *Nature Communications* **2019,** *10*, 1325.

11. Schwille, P.; Spatz, J.; Landfester, K.; Bodenschatz, E.; Herminghaus, S.; Sourjik, V.; Erb, T. J.; Bastiaens, P.; Lipowsky, R.; Hyman, A.; Dabrock, P.; Baret, J. C.; Vidakovic-Koch, T.; Bieling, P.; Dimova, R.; Mutschler, H.; Robinson, T.; Tang, T. Y. D.; Wegner, S.; Sundmacher, K., MaxSynBio: Avenues Towards Creating Cells from the Bottom Up. *Angewandte Chemie-International Edition* **2018,** *57* (41), 13382-13392.

12. Ganzinger, K. A.; Schwille, P., More from Less - Bottom-Up Reconstitution of Cell Biology. *Journal of Cell Science* **2019,** *132* (4), jcs227488.

13. Tsugane, M.; Suzuki, H., Reverse Transcription Polymerase Chain Reaction in Giant Unilamellar Vesicles. *Scientific Reports* **2018,** *8*, 9214.

14. Jahn, R.; Lang, T.; Sudhof, T. C., Membrane Fusion. *Cell* **2003,** *112* (4), 519-533.

15. Chernomordik, L. V.; Zimmerberg, J.; Kozlov, M. M., Membranes of the World Unite! *Journal of Cell Biology* **2006,** *175* (2), 201-207.

16. Lei, G. H.; MacDonald, R. C., Lipid Bilayer Vesicle Fusion: Intermediates Captured by High-Speed Microfluorescence Spectroscopy. *Biophysical Journal* **2003,** *85* (3), 1585-1599.

17. Lira, R. B.; Robinson, T.; Dimova, R.; Riske, K. A., Highly Efficient Protein-free Membrane Fusion: A Giant Vesicle Study. *Biophysical Journal* **2019,** *116* (1), 79-91.

18. Loffler, P. M. G.; Ries, O.; Rabe, A.; Okholm, A. H.; Thomsen, R. P.; Kjems, J.; Vogel, S., A DNA-Programmed Liposome Fusion Cascade. *Angewandte Chemie-International Edition* **2017,** *56* (43), 13228-13231.

19. Nikolaus, J.; Stockl, M.; Langosch, D.; Volkmer, R.; Herrmann, A., Direct Visualization of Large and Protein-Free Hemifusion Diaphragms. *Biophysical Journal* **2010,** *98* (7), 1192-1199.

20. Mora, N. L.; Boyle, A. L.; Kolck, B. J. v.; Rossen, A.; Pokorna, S.; Koukalova, A.; Sachl, R.; Hof, M.; Kros, A., Controlled Peptide-Mediated Vesicle Fusion Assessed by Simultaneous Dual-Colour Time-Lapsed Fluorescence Microscopy. *Scientific reports* **2020,** *10* (1), 3087-3087.

21. Mondal Roy, S.; Sarkar, M., Membrane Fusion Induced by Small Molecules and Ions. *Journal of lipids* **2011,** *2011*, 528784-528784.

22. Bolognesi, G.; Friddin, M. S.; Salehi-Reyhani, A.; Barlow, N. E.; Brooks, N. J.; Ces, O.; Elani, Y., Sculpting and Fusing Biomimetic Vesicle Networks Using Optical Tweezers. *Nature Communications* **2018,** *9*, 1882.

23. Vivek, A.; Bolognesi, G.; Elani, Y., Fusing Artificial Cell Compartments and Lipid Domains Using Optical Traps: A Tool to Modulate Membrane Composition and Phase Behaviour. *Micromachines* **2020,** *11* (4), 388.

24. Rorvig-Lund, A.; Bahadori, A.; Semsey, S.; Bendix, P. M.; Oddershede, L. B., Vesicle Fusion Triggered by Optically Heated Gold Nanoparticles. *Nano Letters* **2015,** *15* (6), 4183-4188.

25. Haluska, C. K.; Riske, K. A.; Marchi-Artzner, V.; Lehn, J. M.; Lipowsky, R.; Dimova, R., Time Scales of Membrane Fusion Revealed by Direct Imaging of Vesicle Fusion with High Temporal Resolution. *Proceedings of the National Academy of Sciences of the United States of America* **2006,** *103* (43), 15841-15846.

26. Tahir, M. A.; Guven, Z. P.; Arriaga, L. R.; Tinao, B.; Yang, Y. S. S.; Bekdemir, A.; Martin, J. T.; Bhanji, A. N.; Irvine, D.; Stellacci, F.; Alexander-Katz, A., Calcium-Triggered Fusion of Lipid Membranes Is Enabled by Amphiphilic Nanoparticles. *Proceedings of the National Academy of Sciences of the United States of America* **2020,** *117* (31), 18470-18476.

27. Lipowsky, R.; Dobereiner, H. G., Vesicles in Contact with Nanoparticles and Colloids. *Europhysics Letters* **1998,** *43* (2), 219-225.

28. Contini, C.; Schneemilch, M.; Gaisford, S.; Quirke, N., Nanoparticle-Membrane Interactions. *Journal of Experimental Nanoscience* **2018,** *13* (1), 62-81.

29. Contini, C.; Hindley, J. W.; Macdonald, T. J.; Barritt, J. D.; Ces, O.; Quirke, N., Size Dependency of Gold Nanoparticles Interacting with Model Membranes. *Communications Chemistry* **2020,** *3* (1), 130.

30. Deserno, M., Elastic Deformation of a Fluid Membrane upon Colloid Binding. *Physical Review E* **2004,** *69* (3), 031903.

31. Nel, A. E.; Madler, L.; Velegol, D.; Xia, T.; Hoek, E. M. V.; Somasundaran, P.; Klaessig, F.; Castranova, V.; Thompson, M., Understanding Biophysicochemical Interactions at the Nano-Bio Interface. *Nature Materials* **2009,** *8* (7), 543-557.

32. Werner, M.; Auth, T.; Beales, P. A.; Fleury, J. B.; Hook, F.; Kress, H.; Van Lehn, R. C.; Muller, M.; Petrov, E. P.; Sarkisov, L.; Sommer, J. U.; Baulin, V. A., Nanomaterial Interactions with Biomembranes: Bridging the Gap between Soft Matter Models and Biological Context. *Biointerphases* **2018,** *13* (2), 028501.

33. Le Bihan, O.; Bonnafous, P.; Marak, L.; Bickel, T.; Trepout, S.; Mornet, S.; De Haas, F.; Talbot, H.; Taveau, J. C.; Lambert, O., Cryo-Electron Tomography of Nanoparticle Transmigration into Liposome. *Journal of Structural Biology* **2009,** *168* (3), 419-425.

34. Zhang, S. W.; Nelson, A.; Beales, P. A., Freezing or Wrapping: The Role of Particle Size in the Mechanism of Nanoparticle-Biomembrane Interaction. *Langmuir* **2012,** *28* (35), 12831-12837.

35. Rautu, S. A.; Orsi, D.; Di Michele, L.; Rowlands, G.; Cicuta, P.; Turner, M. S., The Role of Optical Projection in the Analysis of Membrane Fluctuations. *Soft Matter* **2017,** *13* (19), 3480-3483.

36. Faizi, H. A.; Reeves, C. J.; Georgiev, V. N.; Vlahovska, P. M.; Dimova, R., Fluctuation Spectroscopy of Giant Unilamellar Vesicles Using Confocal and Phase Contrast Microscopy. *Soft Matter* **2020,** *16* (39), 8996-9001.

37. Anderson, T. H.; Min, Y. J.; Weirich, K. L.; Zeng, H. B.; Fygenson, D.; Israelachvili, J. N., Formation of Supported Bilayers on Silica Substrates. *Langmuir* **2009,** *25* (12), 6997-7005.

38. Struck, D. K.; Hoekstra, D.; Pagano, R. E., Use of Resonance Energy Transfer to Monitor Membrane Fusion. *Biochemistry* **1981,** *20* (14), 4093-4099.

39. Ibarguren, M.; Bomans, P. H. H.; Ruiz-Mirazo, K.; Frederik, P. M.; Alonso, A.; Goni, F. M., Thermally-Induced Aggregation and Fusion of Protein-Free Lipid Vesicles. *Colloids and Surfaces B-Biointerfaces* **2015,** *136*, 545-552.

40. Nazemidashtarjandi, S.; Farnoud, A. M., Membrane Outer Leaflet is the Primary Regulator of Membrane Damage Induced by Silica Nanoparticles in Vesicles and Erythrocytes. *Environmental Science-Nano* **2019,** *6* (4), 1219-1232.

41. Ewins, E.; Lira, R. B.; Zhang, W. Y.; Yuan, J. Y.; Antonietti, M.; Robinson, T.; Dimova, R., Poly(Ionic Liquid) Nanoparticles Selectively Disrupt Biomembranes. *Advanced Science* **2019,** *6* (4), 1801602.

42. Strobl, F. G.; Seitz, F.; Westerhausen, C.; Reller, A.; Torrano, A. A.; Brauchle, C.; Wixforth, A.; Schneider, M. F., Intake of Silica Nanoparticles by Giant Lipid Vesicles: Influence of Particle Size and Thermodynamic Membrane State. *Beilstein Journal of Nanotechnology* **2014,** *5*, 2468-2478.

43. Akimov, S. A.; Molotkovsky, R. J.; Kuzmin, P. I.; Galimzyanov, T. R.; Batishchev, O. V., Continuum Models of Membrane Fusion: Evolution of the Theory. *International journal of molecular sciences* **2020,** *21* (11), 3875.

44. Meher, G.; Chakraborty, H., Membrane Composition Modulates Fusion by Altering Membrane Properties and Fusion Peptide Structure. *Journal of Membrane Biology* **2019,** *252* (4-5), 261-272.

45. Wei, X. R.; Jiang, W.; Yu, J. C.; Ding, L.; Hu, J. T.; Jiang, G. B., Effects of SiO2 Nanoparticles on Phospholipid Membrane Integrity and Fluidity. *Journal of Hazardous Materials* **2015,** *287*, 217-224.

46. Wei, X. R.; Yu, J. C.; Ding, L.; Hu, J. T.; Jiang, W., Effect of Oxide Nanoparticles on the Morphology and Fluidity of Phospholipid Membranes and the Role of Hydrogen Bonds. *Journal of Environmental Sciences* **2017,** *57*, 221-230.

47. Kozlovsky, Y.; Chernomordik, L. V.; Kozlov, M. M., Lipid Intermediates in Membrane Fusion: Formation, Structure, and Decay of Hemifusion Diaphragm. *Biophysical Journal* **2002,** *83* (5), 2634-2651.

48. Kozlov, M. M.; Chernomordik, L. V., Membrane Tension and Membrane Fusion. *Current Opinion in Structural Biology* **2015,** *33*, 61-67.

49. Wang, B.; Zhang, L. F.; Bae, S. C.; Granick, S., Nanoparticle-Induced Surface Reconstruction of Phospholipid Membranes. *Proceedings of the National Academy of Sciences of the United States of America* **2008,** *105* (47), 18171-18175.

50. Shillcock, J. C.; Lipowsky, R., Tension-Induced Fusion of Bilayer Membranes and Vesicles. *Nature Materials* **2005,** *4* (3), 225-228.

51. Liu, X. J.; Tian, F. L.; Yue, T. T.; Zhang, X. R.; Zhong, C. L., Pulling Force and Surface Tension Drive Membrane Fusion. *Journal of Chemical Physics* **2017,** *147* (19), 194703.

52. Kliesch, T. T.; Dietz, J.; Turco, L.; Halder, P.; Polo, E.; Tarantola, M.; Jahn, R.; Janshoff, A., Membrane Tension Increases Fusion Efficiency of Model Membranes in the Presence of SNAREs. *Scientific Reports* **2017,** *7*, 12070.

53. Lu, T.; Guo, H. X., How the Membranes Fuse: From Spontaneous to Induced. *Advanced Theory and Simulations* **2019,** *2* (7), 10.

54. Zuraw-Weston, S.; Wood, D. A.; Torres, I. K.; Lee, Y.; Wang, L. S.; Jiang, Z. W.; Lazaro, G. R.; Wang, S. Y.; Rodal, A. A.; Hagan, M. F.; Rotello, V. M.; Dinsmore, A. D., Nanoparticles Binding to Lipid Membranes: From Vesicle-Based Gels to Vesicle Tubulation and Destruction. *Nanoscale* **2019,** *11* (39), 18464-18474.

55. Cevc, G.; Richardsen, H., Lipid Vesicles and Membrane Fusion. *Advanced Drug Delivery Reviews* **1999,** *38* (3), 207-232.

56. Tanaka, T.; Yamazaki, M., Membrane Fusion of Giant Unilamellar Vesicles of Neutral Phospholipid Membranes Induced by La3+. *Langmuir* **2004,** *20* (13), 5160-5164.

57. Wang, L.; Seeley, E. S.; Wickner, W.; Merz, A. J., Vacuole Fusion at a Ring of Vertex Docking Sites Leaves Membrane Fragments within the Organelle. *Cell* **2002,** *108* (3), 357-369.

58. Mattie, S.; McNally, E. K.; Karim, M. A.; Vali, H.; Brett, C. L., How and why Intralumenal Membrane Fragments Form during Vacuolar Lysosome Fusion. *Molecular Biology of the Cell* **2017,** *28* (2), 309-321.

59. Kozlovsky, Y.; Kozlov, M. M., Stalk Model of Membrane Fusion: Solution of Energy Crisis. *Biophysical Journal* **2002,** *82* (2), 882-895.

60. Heo, P.; Park, J. B.; Shin, Y. K.; Kweon, D. H., Visualization of SNARE-Mediated Hemifusion between Giant Unilamellar Vesicles Arrested by Myricetin. *Frontiers in Molecular Neuroscience* **2017,** *10*, 93.

61. Michel, R.; Kesselman, E.; Plostica, T.; Danino, D.; Gradzielski, M., Internalization of Silica Nanoparticles into Fluid Liposomes: Formation of Interesting Hybrid Colloids. *Angewandte Chemie-International Edition* **2014,** *53* (46), 12441-12445.

62. Arribas Perez, M.; Moriones, O. H.; Bastus, N. G.; Puntes, V.; Nelson, A.; Beales, P. A., Mechanomodulation of Lipid Membranes by Weakly Aggregating Silver Nanoparticles. *Biochemistry* **2019,** *58* (47), 4761-4773.

63. Raphael, R. M.; Waugh, R. E., Accelerated Interleaflet Transport of Phosphatidylcholine Molecules in Membranes under Deformation. *Biophysical Journal* **1996,** *71* (3), 1374-1388.

64. Doktorova, M.; Heberle, F. A.; Marquardt, D.; Rusinova, R.; Sanford, R. L.; Peyear, T. A.; Katsaras, J.; Feigenson, G. W.; Weinstein, H.; Andersen, O. S., Gramicidin Increases Lipid Flip-Flop in Symmetric and Asymmetric Lipid Vesicles. *Biophysical Journal* **2019,** *116* (5), 860-873.

65. Gardner, J. M.; Abrams, C. F., Lipid Flip-Flop vs. Lateral Diffusion in the Relaxation of Hemifusion Diaphragms. *Biochimica Et Biophysica Acta-Biomembranes* **2018,** *1860* (7), 1452-1459.

66. Akimov, S. A.; Volynsky, P. E.; Galimzyanov, T. R.; Kuzmin, P. I.; Pavlov, K. V.; Batishchev, O. V., Pore Formation in Lipid Membrane II: Energy Landscape Under External Stress. *Scientific Reports* **2017,** *7* (1), 12509.

67. D'Agostino, M.; Risselada, H. J.; Endter, L. J.; Comte-Miserez, V.; Mayer, A., SNARE-Mediated Membrane Fusion Arrests at Pore Expansion to Regulate the Volume of an Organelle. *Embo Journal* **2018,** *37* (19), e99193.

68. Coomer, C. A.; Carlon-Andres, I.; Iliopoulou, M.; Dustin, M. L.; Compeer, E. B.; Compton, A. A.; Padilla-Parra, S., Single-Cell Glycolytic Activity Regulates Membrane Tension and HIV-1 Fusion. *Plos Pathogens* **2020,** *16* (2), e1008359.

69. Bassereau, P.; Jin, R.; Baumgart, T.; Deserno, M.; Dimova, R.; Frolov, V. A.; Bashkirov, P. V.; Grubmuller, H.; Jahn, R.; Risselada, H. J.; Johannes, L.; Kozlov, M. M.; Lipowsky, R.; Pucadyil, T. J.; Zeno, W. F.; Stachowiak, J. C.; Stamou, D.; Breuer, A.; Lauritsen, L.; Simon, C.; Sykes, C.; Voth, G. A.; Weikl, T. R., The 2018 Biomembrane Curvature and Remodeling Roadmap. *Journal of Physics D-Applied Physics* **2018,** *51* (34), 343001.

70. Risselada, H. J.; Smirnova, Y.; Grubmuller, H., Free Energy Landscape of Rim-Pore Expansion in Membrane Fusion. *Biophysical Journal* **2014,** *107* (10), 2287-2295.

71. Ryham, R. J.; Klotz, T. S.; Yao, L. H.; Cohen, F. S., Calculating Transition Energy Barriers and Characterizing Activation States for Steps of Fusion. *Biophysical Journal* **2016,** *110* (5), 1110-1124.

72. Smirnova, Y. G.; Marrink, S. J.; Lipowsky, R.; Knecht, V., Solvent-Exposed Tails as Prestalk Transition States for Membrane Fusion at Low Hydration. *Journal of the American Chemical Society* **2010,** *132* (19), 6710-6718.

73. Risselada, H. J.; Bubnis, G.; Grubmuller, H., Expansion of the Fusion Stalk and Its Implication for Biological Membrane Fusion. *Proceedings of the National Academy of Sciences of the United States of America* **2014,** *111* (30), 11043-11048.

74. Villanueva, M. E.; Giudice, F.; Ambroggio, E.; Vico, R. V., Liposome Fusion Mediated by Hydrophobic Magnetic Nanoparticles Stabilized with Oleic Acid and Modulated by an External Magnetic Field. *Langmuir* **2021,** *37* (5), 1861-1873.

75. Dasgupta, S.; Auth, T.; Gompper, G., Nano- and Microparticles at Fluid and Biological Interfaces. *Journal of Physics-Condensed Matter* **2017,** *29* (37), 373003.

76. Li, X.; Matino, L.; Zhang, W.; Klausen, L.; McGuire, A. F.; Lubrano, C.; Zhao, W. T.; Santoro, F.; Cui, B. X., A Nanostructure Platform for Live-Cell Manipulation of Membrane Curvature. *Nature Protocols* **2019,** *14* (6), 1772-1802.

77. Lou, H. Y.; Zhao, W. T.; Zeng, Y. P.; Cui, B. X., The Role of Membrane Curvature in Nanoscale Topography-Induced Intracellular Signaling. *Accounts of Chemical Research* **2018,** *51* (5), 1046-1053.

78. Booth, A.; Marklew, C. J.; Ciani, B.; Beales, P. A., In Vitro Membrane Remodeling by ESCRT is Regulated by Negative Feedback from Membrane Tension. *iScience* **2019,** *15*, 173-184.

79. Imam, Z. I.; Kenyon, L. E.; Ashby, G.; Nagib, F.; Mendicino, M.; Zhao, C.; Gadok, A. K.; Stachowiak, J. C., Phase-Separated Liposomes Enhance the Efficiency of Macromolecular Delivery to the Cellular Cytoplasm. *Cellular and Molecular Bioengineering* **2017,** *10* (5), 387-403.

80. Sezgin, E.; Waithe, D.; de la Serna, J. B.; Eggeling, C., Spectral Imaging to Measure Heterogeneity in Membrane Lipid Packing. *Chemphyschem* **2015,** *16* (7), 1387-1394.

81. Kapitza, H. G.; McGregor, G.; Jacobson, K. A., Direct Measurement of Lateral Transport in Membranes by Using Time-Resolved Spatial Photometry. *Proceedings of the National Academy of Sciences of the United States of America* **1985,** *82* (12), 4122-4126.

82. Klapper, Y.; Vranceanu, M.; Ishitsuka, Y.; Evans, D.; Scheider, D.; Nienhaus, G. U.; Leneweit, G., Surface Energy of Phospholipid Bilayers and the Correlation to Their Hydration. *Journal of Colloid and Interface Science* **2013,** *390*, 267-274.

83. Loren, N.; Hagman, J.; Jonasson, J. K.; Deschout, H.; Bernin, D.; Cella-Zanacchi, F.; Diaspro, A.; McNally, J. G.; Ameloot, M.; Smisdom, N.; Nyden, M.; Hermansson, A. M.; Rudemo, M.; Braeckmans, K., Fluorescence Recovery after Photobleaching in Material and Life Sciences: Putting Theory into Practice. *Quarterly Reviews of Biophysics* **2015,** *48* (3), 323-387.